Operational Modal Analysis for Chatter Prediction in Milling

by

Ayberk Zorlu
B.Sc., Middle East Technical University, 2021

A Thesis Submitted in Partial Fulfillment of the
Requirements for the Degree of

MASTER OF APPLIED SCIENCE

in the Department of Mechanical Engineering
University of Victoria

Operational Modal Analysis for Chatter Prediction in Milling

by

Ayberk Zorlu
B.Sc., Middle East Technical University, 2021

Supervisory Committee

Dr. Keivan Ahmadi, Supervisor
(Department of Mechanical Engineering, University of Victoria, Canada)

Dr. Yang Shi, Departmental Member
(Department of Mechanical Engineering, University of Victoria, Canada)

ABSTRACT

Unstable vibrations during machining can harm both the tool and the workpiece, requiring careful selection of process parameters to avoid them. These parameters are usually set based on vibration models of the machining process. However, due to unmodeled dynamics or process variations, chatter can still occur, highlighting the need for online chatter monitoring systems. Existing methods often detect chatter only after it occurs, so there is a need for monitoring systems that can predict chatter before it occurs to ensure high-quality machining.

This thesis presents a new method to identify the dynamics of regenerative chatter from the measured process vibrations in milling. This method combines the synchronous once-per-revolution sampling of stable process vibrations with Operational Modal Analysis to estimate the Floquet multipliers of the delayed linear time-periodic dynamics in milling, all from the natural process vibrations without external excitation. The identified multipliers quantify vibration stability, enabling chatter prediction before it occurs. Additionally, they can be used to calibrate physics-based chatter models based on vibration measurements solely within the stable region.

The method's accuracy in identifying Floquet multipliers is validated through extensive numerical simulations and two experimental case studies. The results show that chatter due to both Hopf and period-doubling bifurcations can be predicted from the process vibrations during stable cuts. Moreover, the experimental case studies demonstrate a vibration measurement system for implementing the presented method in standard milling operations and confirm its effectiveness in practice.

Contents

List of Tables

List of Figures

Acknowledgements

I would like to thank:

Dr. Keivan Ahmadi.
Thank you for believing in me and giving me the opportunity to pursue a master's degree under your supervision. Thank you for your extreme patience and invaluable guidance.

My family and my parents, Kemal & Yeter Zorlu.
Thank you for being with me at every moment and supporting me wholeheartedly. I couldn't have asked for more loving parents.

My fellow Dynamics and Digital Manufacturing Laboratory members: Ali Ebrahimitirtashi, James Duncan McPherson, and Mohammadmahdi Mehrabi.
Thank you for your company along this journey, for sharing your thoughts, and for enriching my path with meaningful discussions.

This research was financially supported by the Natural Sciences and Engineering Research Council of Canada (NSERC).

Dedication

To the most loving mom and dad in the world, Yeter & Kemal Zorlu.

Chapter 1

Introduction

Self-excited vibrations in machining arise from the inherent feedback between the tool, vibrations of the workpiece, and the machining forces that cause them. If the machining parameters are not chosen correctly, these vibrations can become unstable and lead to chatter [4]. Chatter causes critical issues with significant implications on the surface finish of the workpiece, tool longevity, and deterioration of the machine components. Therefore it is essential to maintain stable machining operations to ensure high-quality surface finishes, extend tool life, and preserve the integrity of machine components. As a result, extensive research has been dedicated to understanding machining dynamics, stability, and chatter.

1.1 Problem Statement and Overview of Existing Research

The foundational laws governing chatter stability were established by Tlusty and Polacek [34] and Tobias [35]. Since then, various models in both time and frequency domains have been developed to identify chatter-free machining parameters [5, 6, 9, 16, 21]. The accuracy of the chatter models declines as the dynamics of the machining system change during the process, necessitating regular updates based on in-process sensor feedback.

Accurate chatter prediction requires precise models of the machine tool's structural dynamics, often characterized by its tooltip Frequency Response Function (FRF), and empirical models linking machining parameters to the resulting cutting forces. The tooltip FRF is usually obtained through impulse hammer tests and Experimental Modal Analysis (EMA). Because hammer impulse or shaker excitation cannot be applied during the process, the FRF is measured offline with the spindle off and without machining forces. Consequently, the accuracy of these vibration models diminishes under actual machining

conditions. Similarly, empirical force models, which are also developed offline through extensive testing, lose accuracy when the machining conditions as due to the progression of tool wear evolve. Therefore, it is crucial to update chatter model parameters based on in-process force and vibration measurements to improve accuracy [17, 29].

Since traditional modal testing methods like hammer or shaker tests cannot be applied during machining, an alternative approach uses machining forces as the excitation source to measure the tooltip FRF in-process [28–30]. This method enables real-time vibration model identification but requires a specially designed workpiece to broaden the excitation spectrum due to the periodicity of machining forces at spindle rotation frequencies. Additionally, the industry often avoids using expensive and bulky force dynamometers for measuring cutting forces. Machine learning methods can also be employed to learn stable machining parameters directly from experimental observations during the machining process [13, 14, 24]. However, this top-down approach is limited by the need to collect data during unstable vibration conditions.

Conducting hammer tests or using shakers to identify large structures such as bridges, buildings, airplanes, and ships is impractical. This challenge in system identification for such substantial systems has led to the development of Operational Modal Analysis (OMA). The OMA theory was primarily developed for Linear Time-Invariant (LTI) systems, relying solely on the system's response to extract modal parameters [11]. Hence, there is no need to excite the system under interest via a controlled input such as shakers and impact hammers. OMA identifies the modal parameters of a vibratory system from its response to unmeasured ambient excitation [11]. The output-only approach in OMA is a viable solution for identifying the tool or workpiece's vibration modes from their in-process vibration response, bypassing offline modal tests [2,10,37,38]. Nonetheless, some of the fundamental assumptions in OMA theory are violated in machining, which can lead to misleading results if not addressed appropriately. OMA assumes the ambient excitation is random white noise without feedback from the resulting vibrations. These assumptions are violated in machining because forces include a dominant periodic component at the spindle rotation frequency, and self-excited vibrations create a strong feedback loop. Additionally, the excitation should be random and evenly distributed across space to stimulate all significant modes of the system and extract useful information in OMA. Therefore, OMA results must be interpreted in the context of complex machining system dynamics. In milling operations, the excitation forces occur only at the tool tip and are periodic, apart from the inherent white noise excitation within the machine structure itself. The modes that are prominently present in the output spectrum are of particular interest, as milling stability is primarily influenced by these

modes. This implies that even if the forces are concentrated at the tool tip, the modes under interest are present at the output spectrum.

Self-excited vibrations in turning are described by a closed-loop LTI system with a delay in the feedback loop. Kim and Ahmadi used OMA to identify the dominant pole of the closed-loop system from the tool or workpiece vibrations during operations [25]. These identified poles were later used in a Bayesian algorithm to update chatter model parameters [1]. Unlike data-driven methods, this OMA approach only utilizes data collected under stable conditions. Moreover, the identified pole quantifies the machining process's stability and its distance from instability, providing a critical capability as most existing chatter detection methods only categorize the process as stable or unstable without quantifying stability [15, 20, 27, 31, 33].

Kim and Ahmadi's OMA approach [25] cannot be directly applied to milling vibrations due to the periodic variations in milling dynamics. The dynamics of self-excited vibrations in milling change periodically with the tool's rotation, requiring a closed-loop Linear Time-Periodic (LTP) system model with a delay in feedback. The asymptotic stability of an LTP system is determined by its dominant Floquet multiplier, which cannot be directly identified using OMA methods developed for LTI systems [11]. Kiss et al. disrupted the periodic dynamics by shooting a ball at the milling tool or workpiece and determined the Floquet multiplier from the resulting vibration signal [26]. They demonstrated that in-process impulse responses could accurately estimate theoretical Floquet multipliers, but the method is limited in industrial applications due to safety risks and potential damage to the surface finish or tool from shooting a ball.

This thesis extends Kim and Ahmadi's OMA approach [25] to milling considering its periodic dynamics. The time-periodicity is addressed by employing the lifting technique to build an LTI representation of the LTP system [3, 7, 8, 32, 36]. Subsequently, OMA is applied to identify the poles of the resulting LTI system. We show that the poles of the lifted LTI system are accurate estimations of the LTP system's Floquet multipliers. Numerical simulations with known ground truth are presented to demonstrate the accuracy of the presented method in estimating Floquet multipliers from in-process vibrations. The practical implementation of the method is then demonstrated through two experimental case studies.

1.2 Research Objectives

The main objectives of this thesis are to:

- Use OMA in milling considering its LTP dynamics to quantify the stability level using stable vibration measurements.
- Develop an efficient measurement system to perform OMA.

1.3 Thesis Organization

This thesis will follow the structure as described below:

- Chapter 2 reviews the milling dynamics followed by a discrete time model of the periodic dynamics. Then, the lifting method and the way it is used in OMA is explained. Finally, the details of the Time Domain Poly-Reference (TDPR) method are given.
- Chapter 3 presents a numerical study, with its results compared with the SDM as the ground truth.
- Chapter 4 presents a set of experimental studies including a Single Degree of Freedom (SDOF) case and a Multi Degree of Freedom (MDOF) case, with their results compared with the Semi-Discretization Method (SDM) as the ground truth.
- Chapter 5 highlights the main contributions of this thesis and comments on the possible future works

Chapter 2

Theoretical Background and Literature Review

In this chapter, a Multi Degree of Freedom (MDOF) model of milling dynamics and its stability are discussed. Following this, the implementation of OMA to milling vibrations and the lifting method are explained.

2.1 Milling Dynamics

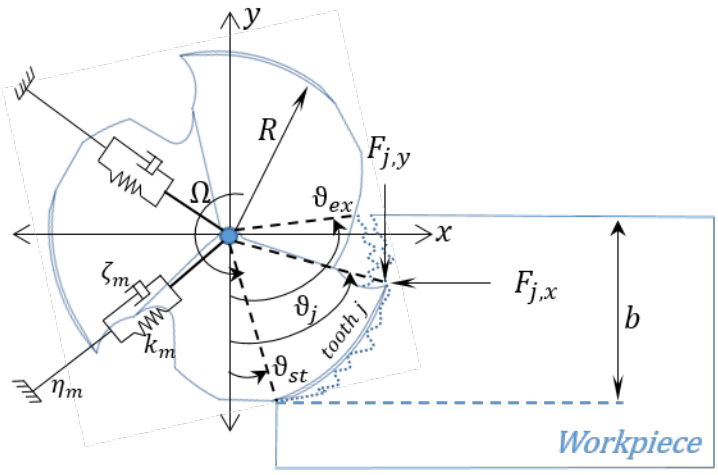

Figure 2.1: Schematic of the forces and chip thickness in milling

Figure 2.1 shows the general MDOF model of the relative tool-workpiece vibrations in milling. The tool has N cutting edges rotating at Ω rad/sec around its axis. The radial width

is denoted b, and the tool radius R. Angular engagement between each tooth and workpiece material starts at ϑ_{st} and ends at ϑ_{ex}. The axial motion is assumed to be rigid and m elastic modes dominate the lateral motion. The equation governing the described motion in the modal space is expressed as follows:

$$\ddot{\boldsymbol{\gamma}}(t) + 2\boldsymbol{\zeta}\boldsymbol{\omega}_n\dot{\boldsymbol{\gamma}}(t) + \boldsymbol{\omega}_n^2\boldsymbol{\gamma}(t) = \boldsymbol{U}^T\boldsymbol{F}_{xy}(t) \tag{2.1}$$

where $\boldsymbol{\zeta} \in \mathbb{R}^{m\times m}$ is diagonal matrix of modal damping ratios, $\boldsymbol{\omega}_n \in \mathbb{R}^{m\times m}$ is the diagonal matrix of natural frequencies, and $\boldsymbol{U} \in \mathbb{R}^{2\times m}$ is the mass normalized mode shape matrix. The tooltip Cartesian deflections, $\boldsymbol{q}(t) = [x(t), y(t)]^T$, are mapped to modal coordinates, $\boldsymbol{\gamma} \in \mathbb{R}^{m\times 1}$, via the mode shapes matrix, as follows:

$$\boldsymbol{q}(t) = \boldsymbol{U}\boldsymbol{\gamma}(t) \tag{2.2}$$

The cutting forces $\boldsymbol{F}_{xy} \in \mathbb{R}^{2x1}$ are periodic at the tooth-passing period, $\tau = \frac{2\pi}{N\Omega}$, and mechanistic models relate them to uncut chip geometry as follows [4]:

$$\mathbf{F}_{xy}(t) = \sum_{j=1}^{N} c_t sin\vartheta_j(t)\boldsymbol{T}_j(t) + \sum_{j=1}^{N} \boldsymbol{T}_j(t)[sin\vartheta_j(t) \quad cos\vartheta_j(t)][\boldsymbol{q}(t) - \boldsymbol{q}(t-\tau)]$$

$$\mathbf{T}_j(t) = ag_j(t)\begin{bmatrix} -K_r sin\vartheta_j(t) - K_t cos\vartheta_j(t) \\ -K_r cos\vartheta_j(t) + K_t sin\vartheta_j(t) \end{bmatrix}; g_j(t) = \begin{cases} 1 & \vartheta_{st} \le \vartheta_j(t) \le \vartheta_{ex} \\ 0 & otherwise \end{cases} \tag{2.3}$$

where a is the axial depth of cut (DOC), K_t and K_r are constant tangential and radial cutting force coefficients, and c_t is the feed motion in mm/rev/tooth. The first term in Eq. 2.3 represents the forces generated by the rigid-body motion of the tool relative to the workpiece, i.e. the feed motion; the second part shows the forces generated by the chip thickness variations due to the phase difference between the tool's elastic deflections in consecutive tooth-passing periods, also known as the regenerative forces. The asymptotic stability of the periodic response of the system in Eq. 2.1 depends on milling parameters, i.e. a, b, and τ. Let the overall modal response $\boldsymbol{\gamma}(t)$ be expressed as the periodic motion $\boldsymbol{\gamma}_p(t)$ disturbed by $\boldsymbol{\eta}(t)$:

$$\boldsymbol{\gamma}(t) = \boldsymbol{\gamma_p}(t) + \boldsymbol{\eta}(t) \tag{2.4}$$

Substituting Eq. 2.4 in Eq. 2.1 leads to the equation of motion of the variational system [18]:

$$\ddot{\boldsymbol{\eta}}(t) + 2\boldsymbol{\zeta}\boldsymbol{\omega}_n\dot{\boldsymbol{\eta}}(t) + \boldsymbol{\omega}_n^2\boldsymbol{\eta}(t) = \boldsymbol{U}^T\boldsymbol{Q}(t)\boldsymbol{U}(\boldsymbol{\eta}(t) - \boldsymbol{\eta}(t-\tau)) \tag{2.5}$$

where $\boldsymbol{Q}(t)$ is the matrix of directional coefficients:

$$\boldsymbol{Q}(t) = \sum_{j=1}^{N} \boldsymbol{T}_j(t)[sin\vartheta_j(t) \quad cos\vartheta_j(t)] \tag{2.6}$$

Alternatively, Eq. 2.5 can be formulated in the following state-space form:

$$\dot{\boldsymbol{\Gamma}}(t) = \boldsymbol{A}(t)\boldsymbol{\Gamma}(t) + \boldsymbol{B}(t)\boldsymbol{\Gamma}(t-\tau) \tag{2.7}$$

where the matrices $\boldsymbol{A}(t)$, $\boldsymbol{B}(t)$, and $\boldsymbol{\Gamma}(t)$ are

$$\boldsymbol{A}(t) = \begin{bmatrix} \mathbf{0}_{[mxm]} & \boldsymbol{I}_{[mxm]} \\ -\boldsymbol{\omega_n^2} + \boldsymbol{U}^T\boldsymbol{Q}(t)\boldsymbol{U} & -2\boldsymbol{\zeta}\boldsymbol{\omega_n} \end{bmatrix}; \boldsymbol{B}(t) = \begin{bmatrix} \mathbf{0}_{[mxm]} & \mathbf{0}_{[mxm]} \\ \boldsymbol{U}^T\boldsymbol{Q}(t)\boldsymbol{U} & \mathbf{0} \end{bmatrix}$$
$$\boldsymbol{\Gamma}(t) = \begin{bmatrix} \boldsymbol{\eta}(t) \\ \dot{\boldsymbol{\eta}}(t) \end{bmatrix} \tag{2.8}$$

2.2 Discrete Time Domain Model

According to the Floquet theorem for periodic Delay Differential Equations (DDE), the characteristic multipliers of the DDE in Eq. 2.7 determine the asymptotic stability of its trivial solution and thereby the periodic vibrations of the tool. However, since the DDE has infinite characteristic multipliers without a closed-form solution, approximate methods are used to determine stability [22]. In this work, we use the updated Semi-Discretization Method (SDM) of Insperger and Stepan [21] to approximate the Floquet multipliers and thereby the system's stability. In SDM, the distributed-parameter system in Eq. 2.7 is approximated by a lumped system after discretizing the delay period into $r \in \mathbb{N}$ intervals of $h = \tau/r$ seconds. The delay term in Eq. 2.7 is assumed to remain constant during each interval, resulting in the following set of ordinary differential equations:

$$\dot{\boldsymbol{\Gamma}}_i = \boldsymbol{A}_i\boldsymbol{\Gamma}_i + \boldsymbol{B}_i\boldsymbol{\Gamma}_{\tau,i} \tag{2.9}$$

where subscript i denotes the corresponding value at $t = ih$, for example, $\boldsymbol{A}(ih) = A_i$, and $\boldsymbol{\Gamma}_{\tau,i}$ is the approximation of the delay term in discrete time notation. The solution of Eq. 2.9 at each discrete time instant leads to a linear map that determines the discretized response at each delay period from its values in the preceding period:

$$z_{i+r} = \mathbf{\Phi} z_i; \quad \mathbf{\Phi} = \boldsymbol{D}_{i+r-1}\boldsymbol{D}_{i+r-2}...\boldsymbol{D}_i \tag{2.10}$$

where z_i is the augmented state vector for $i \geq r$ and $\boldsymbol{D}_i$ is the state transition matrix mapping the state vector to the next discrete time step:

$$z_i = \left[\boldsymbol{\eta}_i^T, \dot{\boldsymbol{\eta}}_i^T, \boldsymbol{\eta}_{i-1}^T, \boldsymbol{\eta}_{i-2}^T, \ldots, \boldsymbol{\eta}_{i-r}^T\right]^T;$$

$$\boldsymbol{D}_i = \begin{bmatrix} \exp(\boldsymbol{A}_i h) & \mathbf{0} & \ldots & \mathbf{0} & (\exp(\boldsymbol{A}_i h) - \boldsymbol{I})\boldsymbol{A}_i^{-1}\boldsymbol{B}_i \\ \boldsymbol{I} & \mathbf{0} & \ldots & \mathbf{0} & \mathbf{0} \\ \mathbf{0} & \boldsymbol{I} & \ldots & \mathbf{0} & \mathbf{0} \\ \vdots & \vdots & \ddots & \vdots & \vdots \\ \mathbf{0} & \mathbf{0} & \ldots & \boldsymbol{I} & \mathbf{0} \end{bmatrix} \tag{2.11}$$

Matrix $\mathbf{\Phi} \in \mathbb{R}^{m(r+1)\times m(r+1)}$ in Eq. 2.10 is the system's monodromy matrix, and its eigenvalues are approximations of the periodic DDE's characteristic multipliers. Due to Floquet theorem, the system in Eq. 2.10 becomes unstable when its monodromy matrix attains an eigenvalue outside of the unit circle on the complex plane [19]. The eigenvalues of the monodromy matrix are also known as the Floquet multipliers.

Vibration stability for a given set of machining parameters (e.g. Spindle speed and DOC) is determined by constructing the transition matrix $\mathbf{\Phi}$ and determining its greatest eigenvalue. The result is usually presented as Stability Lobe Diagrams (SLD) which determine the maximum stable DOC at each spindle speed. In the next section, we show that OMA can identify the milling system's dominant Floquet multiplier from in-process vibration measurements. The identified multiplier can be used to monitor the process stability or to validate the SDM's predictions and update the vibration model accordingly [1].

2.3 Operational Modal Analysis and Lifting Method

Assume the tool's vibrations in X and Y directions are measured r times during each tooth passing period, τ. That is, the fundamental period consists of r number of data points measured by one physical sensor in each direction. The sampling time is then equal to $\Delta t = \tau/r$. With N_c complete cycles (periods) in the entire duration of measurement, the data points collected during the period $c = 1, .., N_c$ can be organized as the following vector:

$$\boldsymbol{M}_c = \left[(\boldsymbol{q}_c^1)^T, (\dot{\boldsymbol{q}}_c^1)^T, (\boldsymbol{q}_c^2)^T, \ldots, (\boldsymbol{q}_c^r)^T\right]^T \tag{2.12}$$

where $\square_c^p$ is the p^{th} set of data points in cycle c. During stable machining conditions, the measured vibrations comprise a periodic motion at the tooth-passing period and a stochastic response due to random excitation that naturally exists in the machining process. Combining these two components, one can express $\boldsymbol{M}_c$ as follows:

$$\boldsymbol{M}_c = \underline{\boldsymbol{U}}\boldsymbol{z}_c + \underline{\boldsymbol{U}}\boldsymbol{S}_c \tag{2.13}$$

where $\boldsymbol{S}_c = \left[(\boldsymbol{\gamma}_{p,c}^1)^T, (\dot{\boldsymbol{\gamma}}_{p,c}^1)^T, (\boldsymbol{\gamma}_{p,c}^2)^T, \ldots, (\boldsymbol{\gamma}_{p,c}^r)^T\right]^T$ is the modal periodic response, $\boldsymbol{z}_c = \left[(\boldsymbol{\eta}_c^1)^T, (\dot{\boldsymbol{\eta}}_c^1)^T, (\boldsymbol{\eta}_c^2)^T, \ldots, (\boldsymbol{\eta}_c^r)^T\right]^T$ is modal stochastic response, and $\underline{\boldsymbol{U}}$ comprises mode shapes:

$$\underline{\boldsymbol{U}} = \begin{bmatrix} \boldsymbol{U} & & \boldsymbol{0} \\ & \boldsymbol{U} & \\ & \ddots & \\ \boldsymbol{0} & & \boldsymbol{U} \end{bmatrix} \tag{2.14}$$

Although the measurement vector in Eq. 2.13 is constructed from two physical sensors, each of its rows can be regarded as the output of a *virtual* sensor that measures the tooltip motion at the same rotation angle during each tooth-passing period. Therefore, the system's periodic variations are not observed when this vector is used as the output of the following *lifted* LTI state-space model:

$$\begin{aligned} \boldsymbol{z}_{c+1} &= \hat{\boldsymbol{\Phi}}\boldsymbol{z}_c + \boldsymbol{\Psi}\boldsymbol{e}_c \\ \boldsymbol{M}_c &= \underline{\boldsymbol{U}}\boldsymbol{z}_c + \underline{\boldsymbol{U}}\boldsymbol{S}_c \end{aligned} \tag{2.15}$$

where $\hat{\boldsymbol{\Phi}}$ is the state transition matrix, $\boldsymbol{\Psi} \in \mathbb{R}^{m(r+1)\times 2r}$ is input distribution matrix, and $\boldsymbol{e}_c \in \mathbb{R}^{2r}$ is the random force in X and Y directions during every period. With the assumption that $\boldsymbol{e}_c$ is independent and identically distributed random, any standard OMA methods can be used to determine the dominant eigenvalues of the state transition matrix, $\hat{\boldsymbol{\Phi}}$, from the output of the virtual sensors in $\boldsymbol{M}_c$. The resulting eigenvalues are estimations of the lifted LTI system's poles; at the same time, the comparison of Eq. 2.15 with Eq. 2.10 makes it evident that they are also estimations of the LTP system's Floquet multipliers.

While other OMA methods can also be used, here we use the Time-Domain Poly Reference (TDPR) method to determine the poles of the lifted LTI system in Eq. 2.15. To this end, we first organize the measured data points in a unified *lifted response* matrix $\boldsymbol{X}$,

where each row shows the signal sampled once-per-tooth-passing by each virtual sensor:

$$\boldsymbol{X} = \begin{bmatrix} x_1^1 & y_1^1 & \dot{x}_1^1 & \dot{y}_1^1 & x_1^2 & y_1^2 & \cdots & x_1^r & y_1^r \\ \vdots & \vdots & \vdots & \vdots & \vdots & \vdots & \vdots & \vdots & \vdots \\ x_{N_c}^1 & y_{N_c}^1 & \dot{x}_{N_c}^1 & \dot{y}_{N_c}^1 & x_{N_c}^2 & y_{N_c}^2 & \cdots & x_{N_c}^r & y_{N_c}^r \end{bmatrix}^T = \begin{bmatrix} \boldsymbol{M}_1 & \dots & \boldsymbol{M}_{N_c} \end{bmatrix} \quad (2.16)$$

Subsequently, we use the TDPR method to estimate the system poles from the Correlation Function (CF) of the lifted signals. The direct estimation of the CF is expressed as follows:

$$\boldsymbol{R}_{\boldsymbol{X}}(c) = \frac{1}{N_c - c} \sum_{k=1}^{N_c - c} \boldsymbol{X}_{*,k} [\boldsymbol{X}_{*,k+c}]^T; \; c = 0 : N_c - 1 \quad (2.17)$$

where $\square_{*,c}$ represents all the rows in column c of the matrix. When the LTI system in Eq. 2.15 is subjected to white random excitation, the CF represents the system's impulse response function scaled by the noise covariance [11]. Therefore, similar to the impulse response function, the CF can be decomposed into modal free decays, as follows:

$$\boldsymbol{R}_{\boldsymbol{X}}(c) = \sum_{p=1}^{2P} \boldsymbol{B}_p \mu_p^c; \; \boldsymbol{B}_p = \boldsymbol{b}_p \boldsymbol{b}_p^T \quad (2.18)$$

where μ_p are the discrete-time poles of the lifted LTI system (also estimates of the Floquet multipliers of the original LTP system). The vectors $\boldsymbol{b}_p$ are the eigenvectors associated with each pole. The total number of $2P$ poles is assumed to dominate the system dynamics.

2.3.1 Auto Regressive (AR) Models and Time Domain Poly Reference (TDPR)

The TDPR method utilizes an auto regressive (AR) model of the CF to identify the system poles. The scaled impulse response is represented by the CF in Eq. 2.18. Hence, the free decay can be expressed using an AR model and the CF [11]:

$$\boldsymbol{R}_{\boldsymbol{X}}(c) = \boldsymbol{A}_1 \boldsymbol{R}_{\boldsymbol{X}}(c-1) + \boldsymbol{A}_2 \boldsymbol{R}_{\boldsymbol{X}}(c-2) + \cdots + \boldsymbol{A}_{na} \boldsymbol{R}_{\boldsymbol{X}}(c - na) \quad (2.19)$$

where $\boldsymbol{A}$ matrices are the AR matrices and na is the order number of the model. Assuming that the CF has N_c number of samples, a block Hankel matrix with na rows can be formed to estimate AR matrices:

$$\boldsymbol{H}_1 = \begin{bmatrix} \boldsymbol{R_X}(1) & \boldsymbol{R_X}(2) & \dots & \boldsymbol{R_X}(c-na) \\ \vdots & \vdots & \ddots & \vdots \\ \boldsymbol{R_X}(na) & \boldsymbol{R_X}(na+1) & \dots & \boldsymbol{R_X}(c-1) \end{bmatrix} \tag{2.20}$$

In addition to this, one block Hankel matrix is required to reconstruct a similar expression as in Eq. 2.19:

$$\boldsymbol{H}_2 = \begin{bmatrix} \boldsymbol{R_X}(na+1) & \boldsymbol{R_X}(na+2) & \dots & \boldsymbol{R_X}(c) \end{bmatrix} \tag{2.21}$$

Hence, for all possible $N_c - na$ values of c, it is possible to construct:

$$\begin{gathered} \boldsymbol{H}_2 = \boldsymbol{A}\boldsymbol{H}_1 \\ \boldsymbol{A} = \begin{bmatrix} \boldsymbol{A}_{na} & \boldsymbol{A}_{na-1} & \dots & \boldsymbol{A}_1 \end{bmatrix} \end{gathered} \tag{2.22}$$

The estimate of the AR matrices, $\hat{\boldsymbol{A}}$, can be performed by forming an overdetermined set of equations. This can be done by taking the transpose of Eq. 2.22:

$$\hat{\boldsymbol{A}} = (\boldsymbol{H}_1^{T+}\boldsymbol{H}_2^T)^T = \boldsymbol{H}_2\boldsymbol{H}_1^+ \tag{2.23}$$

where $\square^+$ represents the pseudo-inverse of the matrix. Eq. 2.22 can be solved using least squared or singular value decomposition method. Depending on the model order, the response can be presented in a discrete state vector $\boldsymbol{U}_d$ that consists of stacked free decay responses:

$$\boldsymbol{U}_d(c) = \begin{bmatrix} \boldsymbol{R}_{\boldsymbol{X}}^T(c-na+1) \\ \vdots \\ \boldsymbol{R}_{\boldsymbol{X}}^T(c-1) \\ \boldsymbol{R}_{\boldsymbol{X}}^T(c) \end{bmatrix} \tag{2.24}$$

A companion matrix, $\boldsymbol{G}$ can be formed using the correlation matrices constructed above, and eigenvalue decomposition can be applied to the companion matrix to find the modal parameters. The companion matrix advances discrete state vector $\boldsymbol{U}_d$ one time step:

$$\boldsymbol{U}_d(c+1) = \boldsymbol{G}\boldsymbol{U}_d(c) \tag{2.25}$$

where the companion matrix $\boldsymbol{G}$ is:

$$\boldsymbol{G} = \begin{bmatrix} \mathbf{0} & \boldsymbol{I} & \mathbf{0} & \mathbf{0} \\ \vdots & \mathbf{0} & \ddots & \vdots \\ \mathbf{0} & \vdots & & \boldsymbol{I} \\ \boldsymbol{A}_{na} & \boldsymbol{A}_{na-1} & \dots & \boldsymbol{A}_1 \end{bmatrix} \tag{2.26}$$

In Eq. 2.26, $\boldsymbol{I}$ and $\mathbf{0}$ are identity and zero matrices of the same size as the auto regressive matrices. It can be shown that eigenvalues of the companion matrix are also eigenvalues of the system in Eq. 2.10 by substituting one term of the decomposed version of the correlation function in Eq. 2.18 into Eq. 2.25:

$$\boldsymbol{G}\boldsymbol{Z}_p = \mu_p \boldsymbol{Z}_p \tag{2.27}$$

where the matrix $\boldsymbol{Z}_p$ is:

$$\boldsymbol{Z}_p = \begin{bmatrix} \boldsymbol{B}_p^T \mu_p^{c-na+1} & \dots & \boldsymbol{B}_p^T \mu_p^{c-1} & \boldsymbol{B}_p^T \mu_p^c \end{bmatrix}^T \tag{2.28}$$

The equivalent continuous-time pole is obtained by $\lambda_p = \frac{\ln \mu_p}{\tau}$, which is usually described by its frequency, $f = \frac{|\lambda_p|}{2\pi}$, and damping ratio, $\zeta = -\mathcal{R}(\lambda_p)/2\pi f$.

2.4 Summary

In this chapter, the mathematical background of milling dynamics was explained in the modal domain which was followed by its discrete-time representation. The stability of the lumped parameter system in the discrete-time domain was discussed. In the following section, the relation between the lifting method, which was employed to express LTP milling dynamics in an LTI frame, and the applicability of OMA to the overall lifted response were investigated. Finally, the details of the Time Domain Poly-Reference method were addressed and it was shown that the eigenvalues of the STM of LTP milling dynamics can be approximated by the eigenvalues of the STM of the LTI overall lifted response using an OMA method.

Chapter 3

Numerical Study

This section presents a set of numerical simulations to validate the accuracy of the proposed OMA approach in identifying the Floquet multipliers of the LTP milling system. Insperger et al. employed a Single Degree Of Freedom (SDOF) test setup to identify chatter frequencies in milling operations [23]. We use the parameters of the same setup in the presented simulations. The test setup in [23] comprises a rigid tool and a compliant work-holding fixture, creating a single flexible mode in the feed X direction with $\omega_n = 920.48 rad/sec$, $\boldsymbol{U}^T = [0.38, 0] kg^{-1}$, and $\zeta = 0.0032$. The tangential and radial cutting coefficients were calibrated experimentally at $K_t = 5.5 \times 10^8 N/m^2$ and $K_r = 2.2 \times 10^8 N/m^2$, respectively. Floquet multipliers of this system were obtained by SDM and used as the ground truth to validate the accuracy of OMA in identifying them from simulated process vibrations.

The stability lobe diagrams of the setup, obtained from the Semi Discretization Method (SDM), are shown in Fig. 3.1b. The block diagram of the numerical simulations is depicted in Fig. 3.1a. The input force consists of periodic machining forces superimposed by broadband white noise to account for the random forces during the process. simulations were conducted in MATLAB Simulink 2023a with fixed $\tau/150$ and $\tau/200$ sec time-steps for 3200 rev/min and 3600 rev/min using ODE45 as the solver. The workpiece displacement response was simulated for N_c=960 tooth-passing periods. It was then combined with random white noise with 10 dB Signal-To-Noise Ratio to account for sensor noise.

Process vibrations were simulated for milling with 3200 and 3600 rev/min spindle speed and various stable DOC values marked with circles on the SLD in Fig. 3.1b. At 3600 rev/min, the stable periodic response goes through period-doubling bifurcation when the DOC exceeds $a = 1.6$ mm. Hopf bifurcation occurs when the DOC exceeds $a = 0.7$ mm at 3200 rev/min. The details of the conducted OMA for two DOC values at 3200 rev/min are demonstrated in Figs. 3.2, 3.3, and 3.4. Similarly, the details of OMA for two DOC values

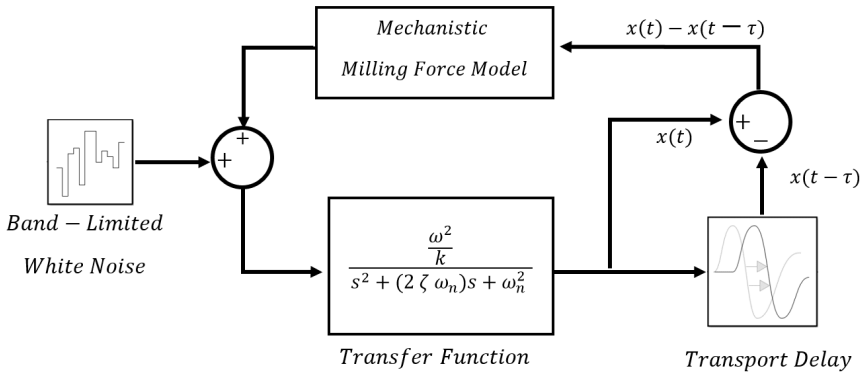

(a)

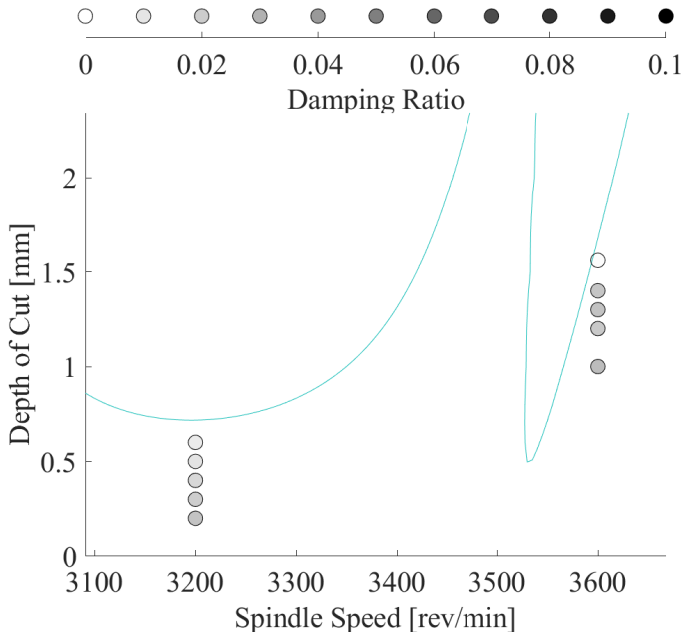

(b)

Figure 3.1: a) Simulink model of the vibrations. b) Stability lobe diagrams of the SDOF setup in [23]. The circles show the simulated points. Five of them are given in Figs. 3.2 to 3.6. The stability border is at 0.7 mm and 1.6 mm for 3200 rev/min and 3600 rev/min, respectively. The unstable points in numerical simulations coincide with SDM results and are not shown.

at 3600 rev/min are shown in Figs. 3.5 and 3.6. The summary of the OMA results for all of the DOC values at these two speeds is presented in Tables 3.1 and 3.2.

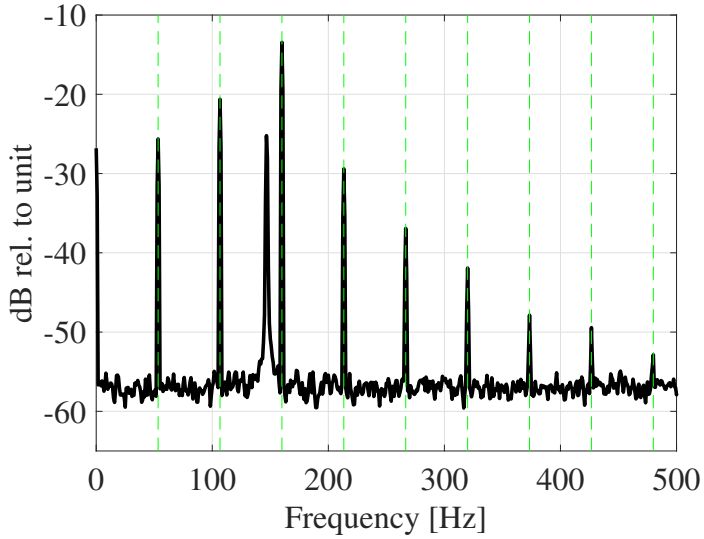

(a)

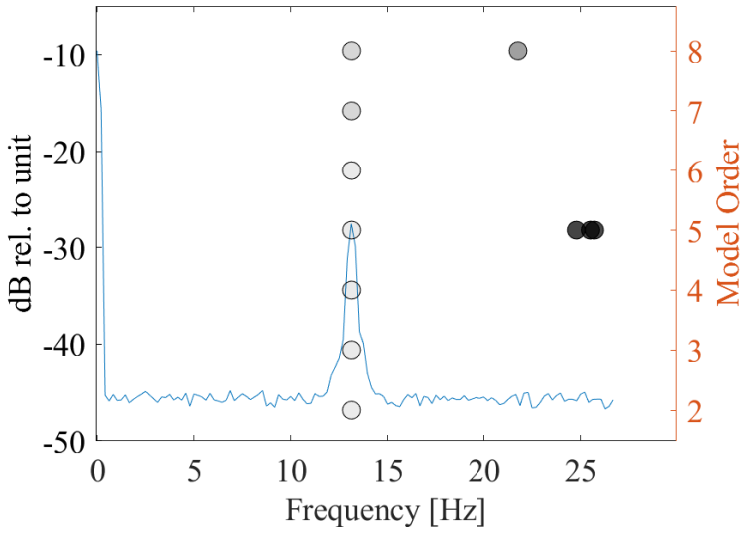

(b)

Figure 3.2: a) Auto PSD of the vibrations at 3200 rev/min, 0.60 mm DOC. Green vertical dashed lines indicate tooth passing frequency and its harmonics. b) Stabilization diagram of the lifted response at 3200 rev/min, 0.60 mm DOC plotted on the singular values of the first channel.

The Power Spectral Density (PSD) of simulated displacement at 3200 rev/min and 0.6 mm depth is displayed in Fig. 3.2a. According to the SLD in Fig. 3.1, at this point, the process is close to the border of stability. The PSD of the simulated vibrations shows peaks at the tooth-passing frequency and its harmonics and a non-harmonic peak at 146.5 Hz.

Fig. 3.2b shows the top singular values of the PSD of the same signal after lifting. The lifted system only includes one peak at around 13 Hz and the tooth-passing harmonics are all eliminated by lifting.

The stabilization diagram resulting from OMA with various model orders (na) is shown in Fig. 3.2b. Following each increase in the model order, the frequencies and damping ratios of the identified poles are compared with their corresponding values from the previous model order. When the two pole's damping ratios are less than 0.05 and vary less than 15%, their frequencies vary less than 0.2%, and the Modal Assurance Criterion (MAC) number of their eigenvectors is above 0.8, the pole is added to the stabilization diagram as a stable pole. The shading of the circles in the stabilization diagram is proportional to the damping of the identified pole, and a streak of circles with similar shading indicates an identified system pole.

The response shows a clear periodic signal prior to lifting, including the tooth passing frequency and its higher harmonics. The only non-harmonic peak observed in Fig. 3.2a occurs at 146.5 Hz. On the other hand, there is just a single peak in the lifted response in Fig. 3.2b, free of any periodicity, corresponding to the dominant pole of the system. Figs. 3.2 to 3.6 display the stabilization diagrams of five different cases obtained by the TDPR identification process. These five cases are also represented in Fig. 3.1 with circles indicating the respective damping ratios of the identified stable poles. Even with a low-order model, the dominant poles are successfully identified in all five cases.

Nyquist frequency of the lifted signal for a single flute cutter is $f_n = 1/2\tau$, which equates to 26.67 Hz for the test at 3200 rev/min. According to the Floquet theorem, the response spectrum comprises frequencies $(f_c \pm nf_{tp})$ and $(-f_c \pm nf_{tp})$, where f_c represents the oncoming chatter frequency, f_{tp} denotes the tooth passing frequency, and n stands for any integer number [23]. Considering that the response before lifting shows a chatter frequency of 146.5 Hz, the 13 Hz peak corresponds to $-f_c + 3f_{tp}$. The identified pole has a (mean) frequency of $f = 13.13$ Hz and a damping ratio of $\zeta = 0.0081$. The corresponding continuous time pole is $-0.668 + 82.495i$, and the corresponding discrete-time pole is $\mu_p = e^{\lambda_p \tau} = 0.024 + 0.987i$. A negligible variance was noted in the frequency, and the standard deviation of the damping ratio was 0.01%. The identified pole's modulus is $|\mu| = 0.988$, suggesting proximity to the stability border. The dominant eigenvalue of the monodromy matrix was determined using SDM with the same discretization interval $(\tau/150)$ as the simulated lifted signal [21]. The discrete-time pole was found to be 0.027 + 0.991i, When converted to continuous time, it corresponds to a frequency of $f = 13.10$ Hz and a damping ratio of $\zeta = 0.0054$.

Depth of cut [mm]	Method	f [Hz]	SD	ζ [mean]	SD	μ_p	$\|\|\mu_p\|\|$
0.2	SDM	13.37	-	0.0246	-	-0.003 + 0.962i	0.962
	OMA	13.49	0.0843	0.0228	0.0035	-0.017 + 0.964i	0.964
0.3	SDM	13.30	-	0.0197	-	0.004 + 0.969i	0.969
	OMA	13.37	0.0221	0.0196	0.0009	-0.004 + 0.969i	0.969
0.4	SDM	13.23	-	0.0150	-	0.012 + 0.977i	0.977
	OMA	13.27	0.0075	0.0136	0.0009	0.007 + 0.979i	0.976
0.5	SDM	13.17	-	0.0101	-	0.019 + 0.984i	0.984
	OMA	13.21	0.0062	0.0101	0.0004	0.014 + 0.984i	0.984
0.6	SDM	13.10	-	0.0054	-	0.027 + 0.991i	0.992
	OMA	13.13	0.0028	0.0081	0.0001	0.024 + 0.987i	0.988

Table 3.1: Comparison of the identified poles with the SDM results, 3200 rpm

A similar analysis was performed for a set of DOC values at 3200 rev/min, and the results show good agreement with SDM predictions, as summarized in Table 3.1. The results at a depth of 0.5 mm and 0.2 mm are also given in Figs. 3.3 and 3.4, respectively. The identified modulus for the 0.5 mm case was 0.9833, indicating that there is still a distance from the stability border before the process becomes completely unstable parallel to the results at 0.6 mm. It can easily be seen that the damping ratio gets bigger as the depth of cut decreases throughout Figs. 3.2 and 3.4, accurately represented by the shading of the circles plotted on the lifted responses. This trend reflects itself in the magnitude of the discrete-time pole; hence, it is possible to comment on the stability level of these processes by looking at the modulus. The modulus of the identified discrete time pole at 0.2 mm is 0.9632, which agrees that the point is far away from the border.

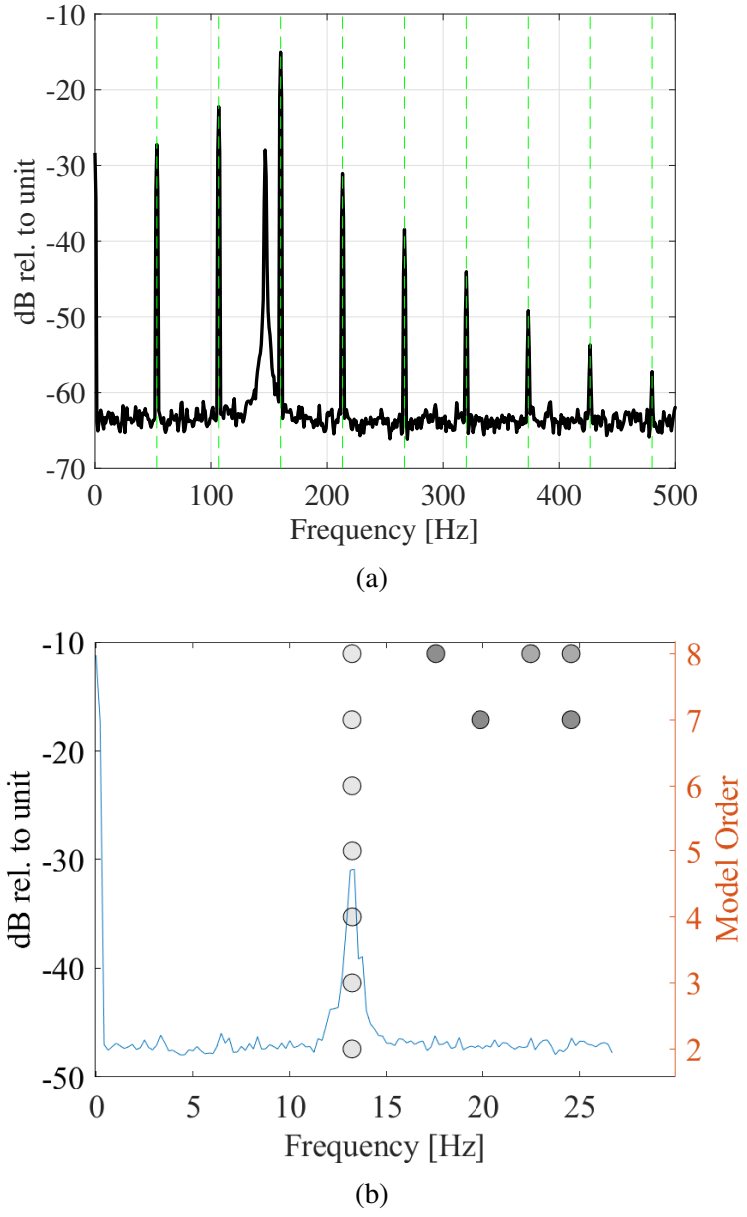

Figure 3.3: a) Auto PSD and b) the stabilization diagram of the lifted response, 0.5 mm DOC at 3200 rev/min

Figs. 3.5a and 3.6a show the PSD of the simulated displacement at 3600 rev/min and 1.56 mm and 1 mm DOC, respectively. Simulations were carried out with a discretization interval of $h = \tau/200$, resulting in a lifted response with 200 channels (rows in $\boldsymbol{X}$). Aside from the expected tooth-passing frequency harmonics, the simulated vibrations exhibit peaks near the natural frequency. At 1.56 mm DOC, which is closer to the stability border, the PSD includes additional (side-band) peaks at the natural frequency plus and minus

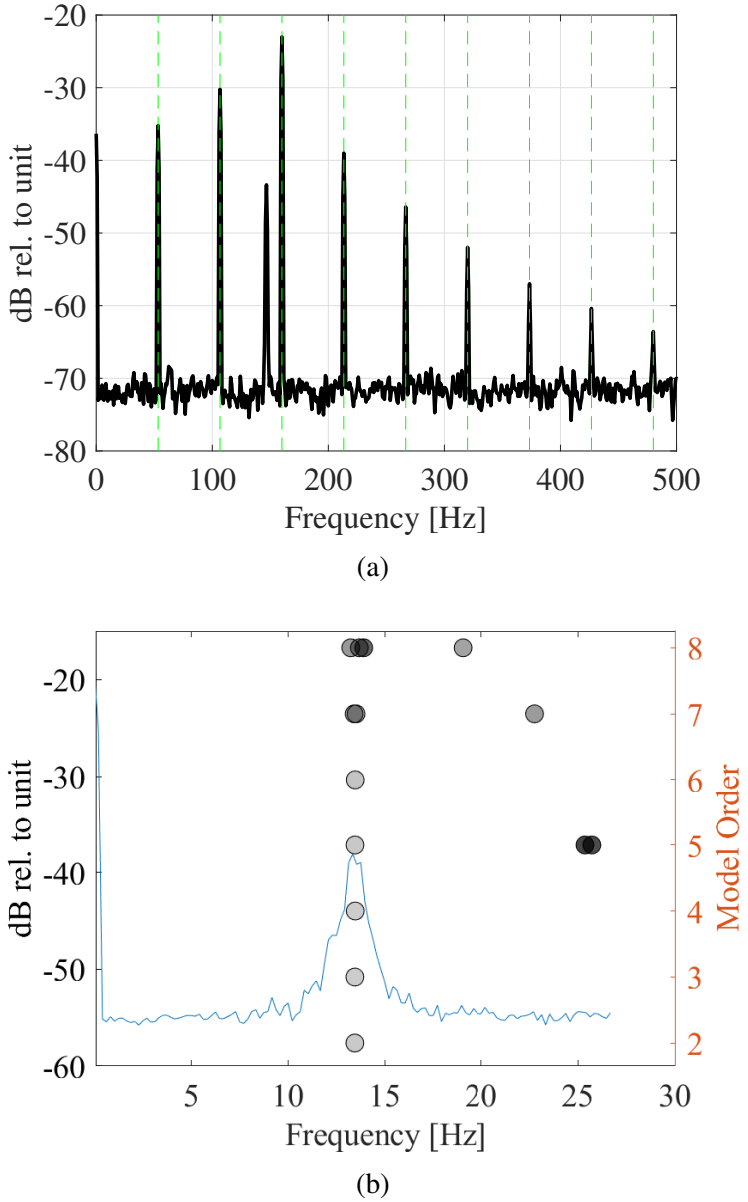

Figure 3.4: a) Auto PSD and b) the stabilization diagram of the lifted response, 0.2 mm DOC at 3200 rev/min

integer multiples of the tooth-passing frequency [23]. The OMA stabilization diagram for each case is also shown in the corresponding figure. The lifted response shows a clear peak that approaches the Nyquist frequency as the DOC approaches the stability border. Despite being very close to the Nyquist frequency, both of the peaks are identified by OMA. At 1 mm DOC, the consistent streak of circles at 28.23 Hz indicates a stable pole.

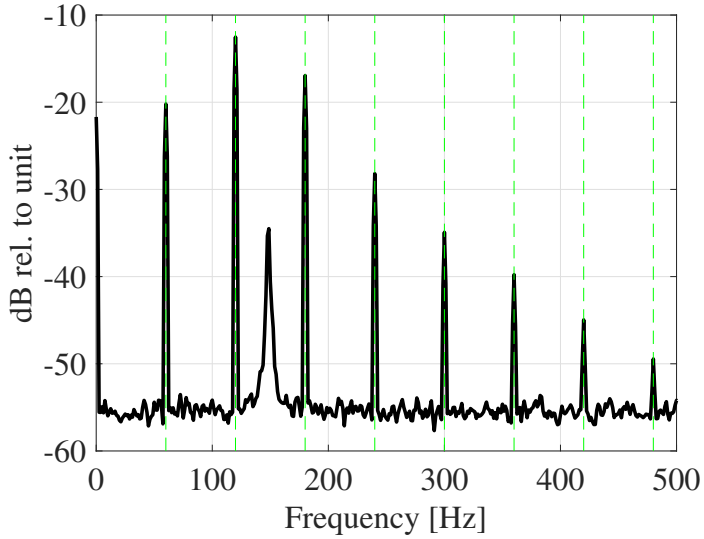

(a)

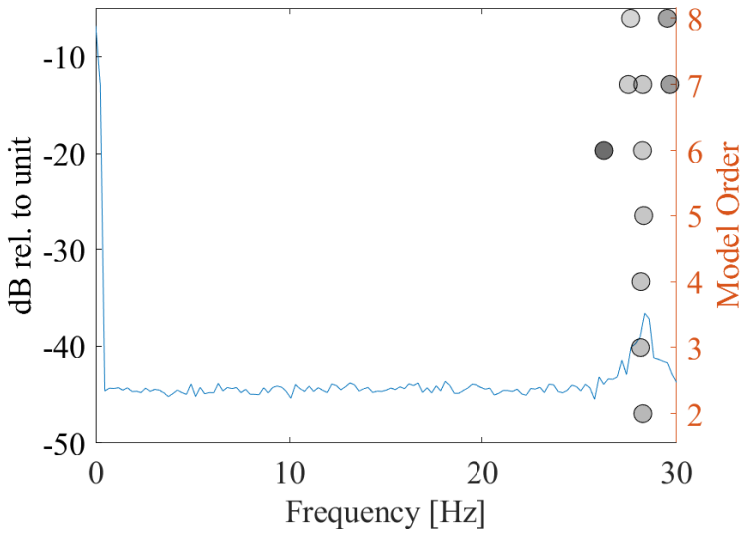

(b)

Figure 3.5: a) Auto PSD and b) the stabilization diagram of the lifted response, 1.0 mm DOC at 3600 rev/min.

This pole has a frequency of 28.23 Hz with a damping ratio of 0.0235, equivalent to a discrete-time pole of $-0.917 + 0.173i$ with a modulus of 0.933. The SDM eigenvalue of the monodromy matrix is $-0.915 + 0.176i$ with a modulus of 0.932 corresponding to 28.18 Hz and a damping ratio of 0.0235. At 1.56 mm, OMA identifies a pole with 30Hz frequency and 0.0012 damping, corresponding to discrete-time pole μ_p=-0.996, which is in good agreement with SDM prediction of μ_p=-0.991.

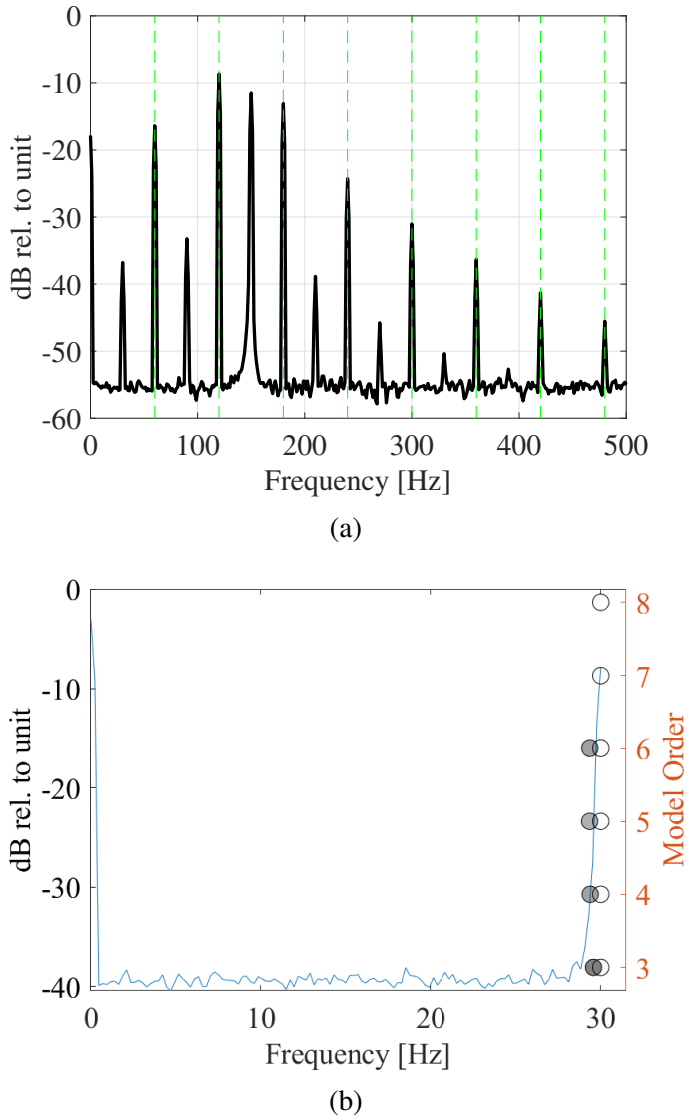

Figure 3.6: a) Auto PSD and b) the stabilization diagram of the lifted response, 1.56 mm DOC at 3600 rev/min.

As we approach the stability border, the oncoming chatter frequency tends to approach the Nyquist frequency of the lifted response. This trend is evident in the behavior of the singular values shown in Figure 3.6b while the oncoming chatter frequency is situated right in between the harmonics in Figure 3.6a. Singular values peak at a frequency very close to the Nyquist frequency, 30 Hz, and a pole with a very low damping value was identified at this frequency. The estimated modulus of 0.996 suggests that this process is on the verge of becoming unstable.

A similar analysis was performed for the simulated signals at a set of DOC values at

3600 rev/min and the summary of the results is shown in Table 3.2. As is expected in period-doubling bifurcation, by increasing the DOC, the poles identified by the OMA and predicted by SDM approach -1. Furthermore, the close agreement of the OMA-identified poles with the SDM-predicted poles shows the accuracy of the proposed approach in identifying the Floquet multipliers during the process. Nonetheless, to implement this method in practice, vibrations must be sampled synchronously with tooth-passing, which requires a relatively complex measurement setup and may cause inaccuracies in identification. The experimental study in the next section demonstrates the implementation of the method and studies its accuracy and effectiveness in practice.

Depth of cut [mm]	Method	f [Hz]	SD	ζ [mean]	SD	μ_p	$\|\|\mu_p\|\|$
1.0	SDM	28.18	-	0.0237	-	-0.915 + 0.176i	0.932
	OMA	28.23	0.0632	0.0235	0.0024	-0.917 + 0.173i	0.933
1.2	SDM	28.64	-	0.0241	-	-0.921 + 0.133i	0.930
	OMA	28.49	0.0577	0.0220	0.0075	-0.925 + 0.148i	0.936
1.3	SDM	28.91	-	0.0241	-	-0.923 + 0.106i	0.930
	OMA	29.1	0.0432	0.0225	0.0039	-0.929 + 0.088i	0.934
1.4	SDM	29.6	-	0.0236	-	-0.929 + 0.040i	0.930
	OMA	29.21	0.181	0.0226	0.0043	-0.930 + 0.078i	0.933
1.56	SDM	30	-	0.0029	-	-0.991	0.991
	OMA	30	7e-7	0.0012	0.0004	-0.996	0.996

Table 3.2: Comparison of the identified poles with the SDM results, 3600 rpm

3.1 Summary

In this chapter, the proposed method was tested on the simulation data. The SDOF case in [23] was simulated, and the displacement response of the system was lifted. The poles identified by the OMA were compared with the SDM results as the ground truth. Two different bifurcation types, Hopf and Period Doubling, were identified successfully along with the dominant poles' frequencies and damping ratios.

Chapter 4

Experimental Results

This section presents two experimental case studies to demonstrate the accuracy of the proposed method in practice and its practical implementation. In the first case, a 6061-T6 aluminum workpiece mounted on a monolithic uni-directional aluminum flexure was milled by a 12.7 mm diameter 2-fluted solid carbide endmill, as shown in Fig. 4.1a. The flexure's compliance in normal and axial directions is negligible, and its deflection in the feed direction is dominated by one mode. The tool's compliance compared to the flexure is also negligible. The relative vibrations of the tool and workpiece are therefore accurately modeled by a SDOF system. Considering the simple dynamics of this setup, SDM yields accurate predictions of the Floquet multipliers, which will be used as ground truth to validate the accuracy of OMA estimations. The second case represents a standard milling setup where a rigid Al 6061-T6 workpiece is milled by a flexible 2-fluted endmill.

In the first (SDOF) case, vibrations are measured by a piezoelectric accelerometer (PCB 352C22) attached directly to the flexure. In the second (MDOF) case, two piezoelectric accelerometers of the same model (PCB 352C22) are attached to the stationary part of the spindle nose. In both cases, a hall-effect sensor provides the trigger signal for the Synchronous sampling in dSPACE MicroLabBox, as shown in Fig. 4.1b. The Hall-Effect sensor was fixed to the non-rotating part of the spindle and a magnet was attached to the rotating part. Two trigger conditions were defined in MicroLabBox to acquire a constant number of data points at 5.0×10^{-5} seconds every time the Hall-Effect sensor generates a rising edge. With this setup, data acquisition starts precisely when the magnet passes in front of the Hall-Effect sensor. Therefore, the accelerometer's analog signal is sampled at the same tool rotational angles in each period. The number of data points after each trigger is determined by the tooth-passing period and the sampling period. For example, with a spindle speed of 2400 rev/min and a sampling period of 5.0×10^{-5} seconds, 250

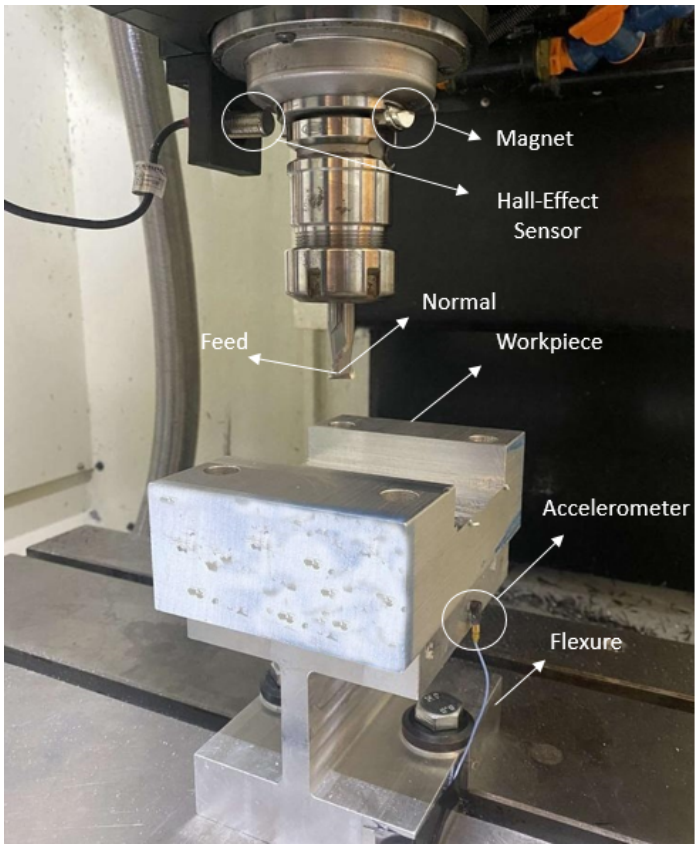

(a)

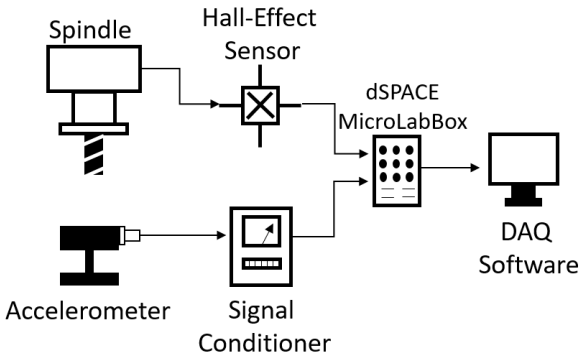

(b)

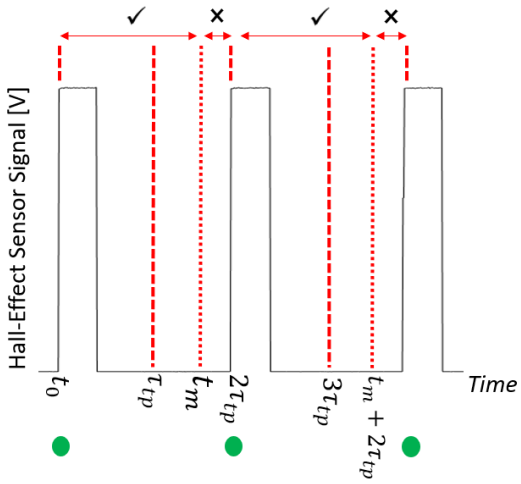

(c)

Figure 4.1: a) The experimental setup. Hall-Effect sensor is attached to the stationary part of the spindle. The SDOF flexure was bolted to the table. b) Equipment configuration of the data acquisition, c) data acquisition procedure integrated with the Hall-Effect sensor.

points are captured in every tooth-passing period of a 2-flute cutter. Ideally, data for every tooth-passing period should be fully measured, generating 500 points after each rising edge. However, completely sampling every tooth-passing period may not be possible because the data acquisition (DAQ) system requires processing time before the start of the next trigger. A simple yet effective solution is to acquire the maximum number of data points, including a full tooth-passing period and most of the second tooth-passing period. For example, by collecting 480 points at 2400 rev/min, the DAQ system has enough time to process all the information before the next trigger. With 480 points in each trigger, the first 230 points in each tooth-passing period can be recorded, which is sufficient for performing OMA. A visual representation of the data acquisition logic is illustrated in Fig. 4.1c, where green dots show the start of acquisition, check marks show the acquisition intervals, and the crosses show the interval of no acquisition where the DAQ waits for the next trigger. t_m is the discrete-time instant corresponding to the maximum number of data points collected after each trigger. In all of the experiments, the machining sound was also sampled continuously by a microphone.

The same workpiece material and tool were used in both experimental cases. Tangential and radial cutting coefficients were determined by orthogonal to Oblique transformation method at $K_t = 650\ \mathrm{N/m^2}$ and $K_r = 110\ \mathrm{N/m^2}$, respectively [12].

The SDM predictions of the Floquet multipliers are close to the poles that OMA identifies in both the Hopf bifurcation cases, shown in Tables 4.1 and 4.2, and period-doubling bifurcation case, shown in Tables 4.3. The observed level of accuracy is partly owed to the simple dynamics of this SDOF case. The system dynamics in this case are dominated by a single mode that can be measured by an impulse hammer and remains relatively unchanged throughout the process. This is not usually the case in standard machining operations where the tool is flexible in both lateral directions and its dynamics during the process are different than those measured offline by hammer tests. The MDOF experimental case in the next section compares the SDM predictions with the OMA estimations in a standard milling process.

4.1 SDOF Case

Before removing any material from the workpiece, the modal parameters of the flexure and the workpiece assembly in the feed direction were determined by impulse hammer tests as $\omega_n = 195.3 \times 2\pi$ rad/sec, $\boldsymbol{U}^T = [0.64, 0]kg^{-1}$, and $\zeta = 0.004$. The stability diagram obtained by the SDM is shown in Fig. 4.2a. Three sets of full-immersion experiments were

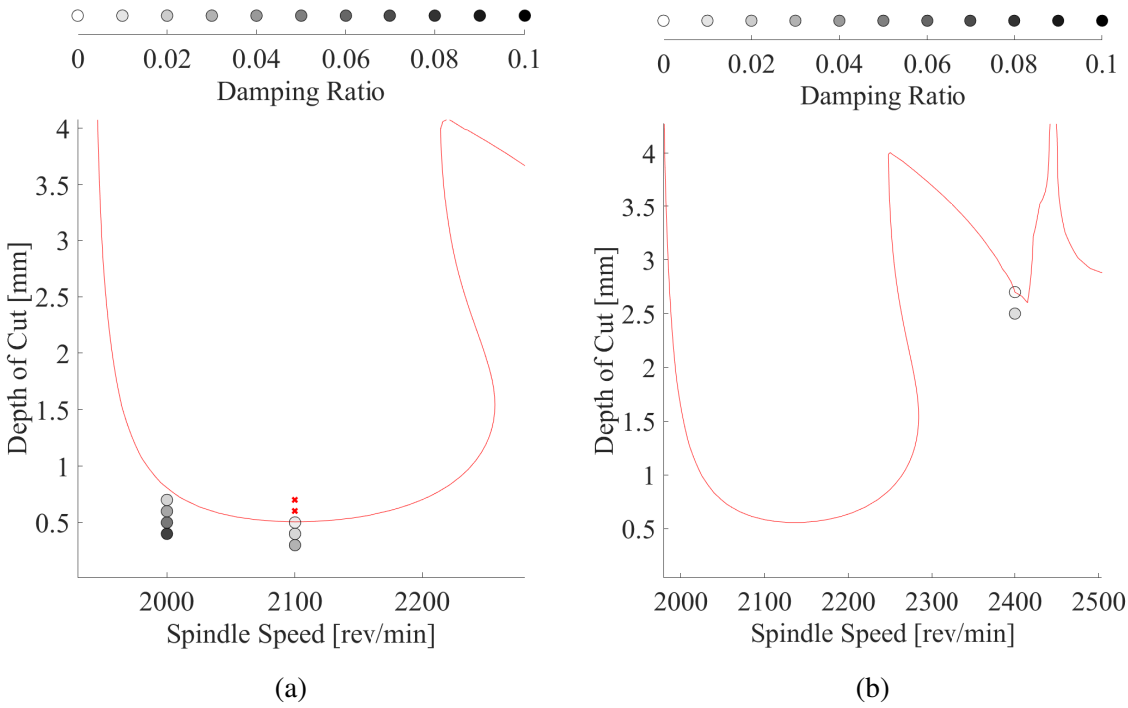

Figure 4.2: Stability Lobes Diagram obtained by SDM. The number of discretization intervals is 40.

performed at 2000, 2100, and 2400 rev/min and several DOC values at each spindle speed. The tested DOC at 2000 and 2100 rev/min are marked with circles and crosses in Fig. 4.2, where circles indicate stable cuts and crosses unstable. A significant amount of material had been removed after completing the tests at 2000 and 2100 rev/min, causing a considerable change in the system's modal parameters. At that point, the new modal parameters were measured again by impulse hammer tests at $\omega_n = 196.35 \times 2\pi$ rad/sec and $\zeta = 0.55\%$ without a significant change in stiffness. The SLD of the system with updated parameters is shown in Fig. 4.2b. The full-immersion cuts at 2400 rev/min were then performed at the DOC values shown in the same figure. Notably, a period-doubling domain behavior was identified at 2400 rev/min, aligning with expectations after accounting for the changes in the system parameters, and the results were plotted in Fig. 4.2b. The changes in the parameters and the shift in characteristics highlight the importance of in-process monitoring.

Figs. 4.3 and 4.4 show the OMA stabilization diagrams for two measurements at 2000 rev/min. The figure also shows the PSD of the measured machining sound. In both cases, vibrations are stable and the sound spectrum is dominated by tooth-passing frequency harmonics. The tooth-passing period, calculated as 0.0150 seconds, necessitated

the collection of 300 data points to capture the entire tooth-passing period, given a sampling time of 5.0×10^{-5} seconds. 500 samples were collected after every rising edge of the Hall effect sensor. Hence, 200 channels can be constructed in the lifted response.

DOC [mm]	Method	f [Hz]	SD	ζ [mean]	SD	μ_p	$\|\|\mu_p\|\|$
0.4	SDM	4.62	-	0.0855	-	0.87 + 0.41i	0.963
	OMA	3.89	0.0182	0.0858	0.0143	0.90 + 0.35i	0.970
0.5	SDM	4.59	-	0.0670	-	0.88 + 0.41i	0.972
	OMA	3.97	0.0222	0.0589	0.0157	0.91 + 0.36i	0.978
0.6	SDM	4.55	-	0.0488	-	0.89 + 0.41i	0.979
	OMA	4.84	0.0362	0.0409	0.0133	0.88 + 0.43i	0.982
0.7	SDM	4.50	-	0.0311	-	0.90 + 0.41i	0.987
	OMA	3.81	0.0233	0.0276	0.0066	0.93 + 0.35i	0.990
0.8	SDM	4.46	-	0.0139	-	0.91 + 0.41i	0.994
	OMA	Unstable					

Table 4.1: Identified poles at 2000 rev/min.

The dominant mode for 0.4 mm shows itself at 196 Hz in Fig. 4.3a, aligning closely with the natural frequency of the setup. As previously demonstrated, the periodic system response exhibits peaks at $(f_c \pm n f_{tp})$ or $(-f_c \pm n f_{tp})$ in its spectrum. The lifted response, on the other hand, includes information up until its Nyquist frequency at $1/2\tau$, where $f_c = 196$ Hz and $f_{tp} = 66.67$ Hz for a 2-flute cutter. In this specific case, the Nyquist frequency is 33.33 Hz, and a peak is expected at approximately $(-f_c + 3 \times f_{tp})$ = 4 Hz. The PSD of the lifted vibration signals also shows a clear peak at around 5 Hz, which is identified as a stable pole by the TDPR method in Fig. 4.3b. The identified pole has a frequency of 3.89 Hz and a damping ratio of 0.0858. The dominant pole from the SDM reads 4.62 Hz and 0.0855 for the frequency and damping ratio, respectively. The modulus of the identified pole is 0.97 suggesting that the DOC can be further increased in the stable region. 0.7 mm DOC at the same spindle speed resulted in a stable cut very close to the stability border. Fig. 4.4a shows the PSD of the sound pressure, and the process is close to being marginally stable where the frequency and the damping ratio of the identified continuous time pole are 3.81 Hz and 0.0276, respectively. This corresponds to $\mu = 0.93 + 0.35i$ in discrete time with a modulus of 0.990. It is seen that the stabilization diagrams in experiments include more spurious modes than the numerical simulation cases.

DOC [mm]	Method	f [Hz]	SD	ζ [mean]	SD	μ_p	$\|\|\mu_p\|\|$
0.3	SDM	14.20	-	0.0247	-	0.28 + 0.92i	0.969
	OMA	10.56	0.0889	0.0223	0.0047	0.57 + 0.80i	0.979
0.4	SDM	14.04	-	0.0124	-	0.30 + 0.94i	0.984
	OMA	11.23	0.0102	0.0104	0.0063	0.53 + 0.84i	0.989
0.5	SDM	13.87	-	0.0006	-	0.31 + 0.95i	0.999
	OMA	11.47	0.0041	0.0064	0.0037	0.51 + 0.85i	0.993
0.6	SDM	Unstable					
	OMA	Unstable					

Table 4.2: Identified poles at 2100 rev/min.

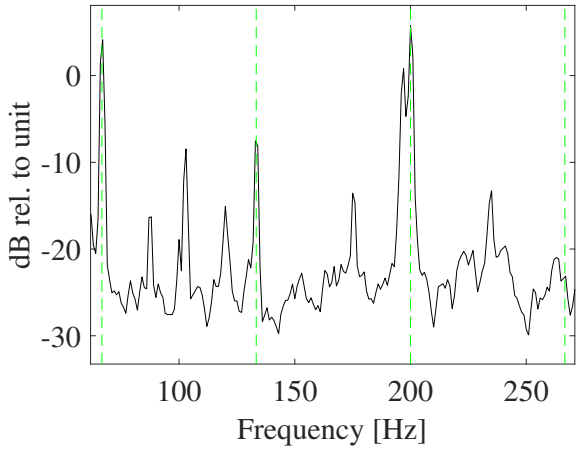

(a)

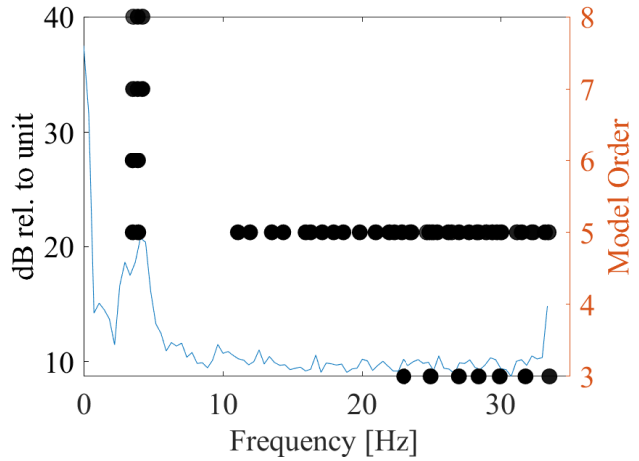

(b)

Figure 4.3: Auto PSD of the machining sound (a), and stabilization diagram (b) for: 0.4 mm at 2000 rev/min

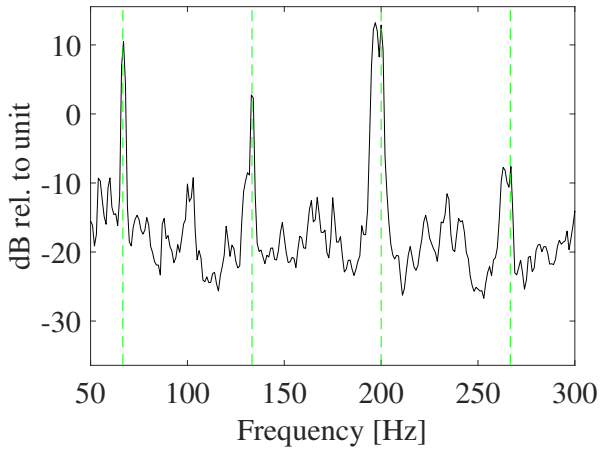

(a)

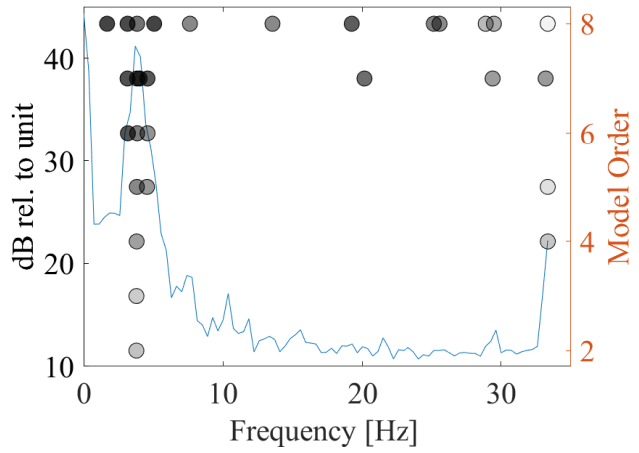

(b)

Figure 4.4: Auto PSD of the machining sound (a) and stabilization diagram (b) for: 0.7 mm at 2000 rev/min

Another Hopf bifurcations case was encountered at 2100 rev/min. The tests were conducted starting from 0.3 mm DOC up to 0.6 mm DOC. The sound PSD and identification results for 0.5 mm are depicted in Fig. 4.5. The PSD of the machining sound revealed a dominant peak at 198.66 Hz. This dominant peak was isolated using the lifted method, and the lifted response, expressed in an LTI frame, has the same mode at 11.47 Hz. The parameters of the continuous time pole were found using the OMA, which resulted in $\zeta = 0.0064$ and $f = 11.47$ Hz. This corresponds to $0.51 + 0.85i$ in the discrete time with a modulus of 0.993. The process became unstable at 0.6 mm, parallel to the identified modulus at 0.5 mm which is very close to 1. The PSD of the machining sound at 0.6 mm is

also given in Fig. 4.5c where the frequency spectrum is dominated by the chatter response.

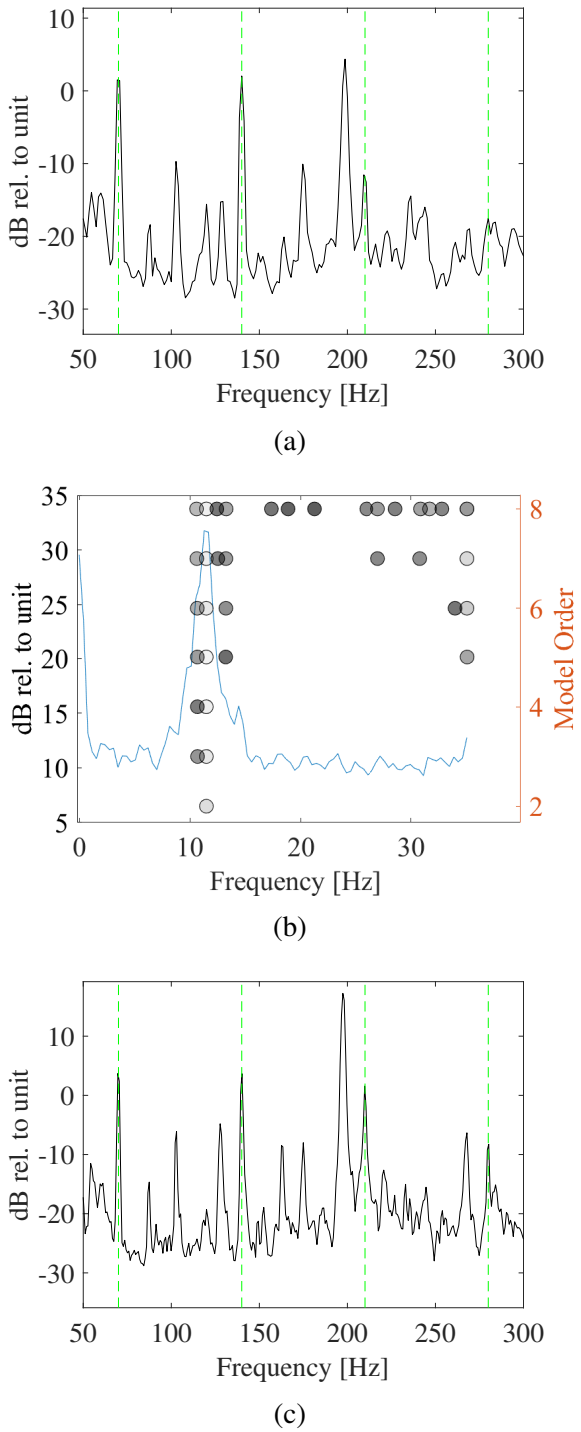

Figure 4.5: a) Auto PSD of the machining sound, b) stabilization diagram of the lifted response at 0.5 mm, 2100 rev/min. c) shows the auto PSD of the machining sound for the unstable operation at 0.6 mm, 2100 rev/min

A similar analysis was conducted for all of the points shown in Fig. 4.2 and the summary of the results along with a comparison with SDM predictions are presented in Tables 4.1, 4.2 and 4.3. Figs. 4.6 and 4.7 show the stabilization diagrams for the measurements at 2400 rev/min. According to the SLD, at this speed, system dynamics go through period-doubling bifurcation when DOC exceeds $a = 2.8$ mm. In both of the tested DOC values, the PSD of the lifted signal shows peaks adjacent to Nyquist frequency, which is expected in period-doubling bifurcation. The tooth-passing periods, computed as 0.0125 seconds required collecting 250 data points to cover the entire period, considering a sampling time of 5.0×10^{-5} seconds. The maximum number of data points to capture the first tooth pass and most of the second tooth pass without missing any triggers was found to be 480. Hence, 230 points in each tooth passing period can be included in the overall lifted response $\boldsymbol{X}$ for identification.

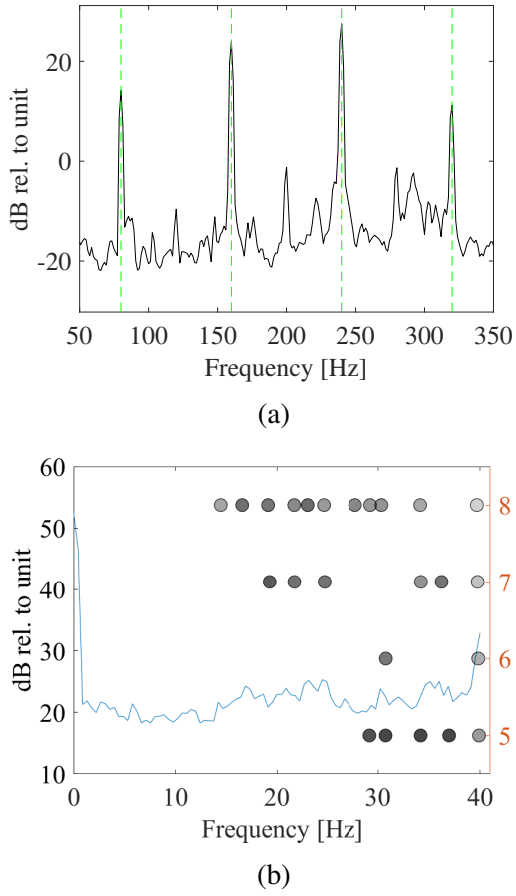

Figure 4.6: Auto PSD of the machining sound (a), stabilization diagrams (b) for: 2.5 mm at 2400 rev/min

As the depth of cut approaches the stability border in the period-doubling domain, the identified discrete time poles are expected to converge to -1 [23]. Fig. 4.6 shows the auto-PSD of the sound signal, the stabilization diagram, and the comparison of the measured and estimated correlation functions for 2.5 mm at 2400 rev/min. The auto-PSD in Fig. 4.6a reveals the impending chatter frequency around 200 Hz, positioned between two harmonics. Consequently, the lifted response in Fig. 4.6b features a dominant peak arising from the least stable pole at the Nyquist frequency, 40 Hz in this instance, calculated using the relation $(f_c - nf_{tp})$ with f_{tp}= 80 Hz and f_c= 200 Hz for n=3. The TDPR is able to identify a stable pole close to 40 Hz in both cases at 2.5 mm and 2.7 mm. The comparison of the identified poles with SDM predictions in this period-doubling case is presented in Table 4.3.

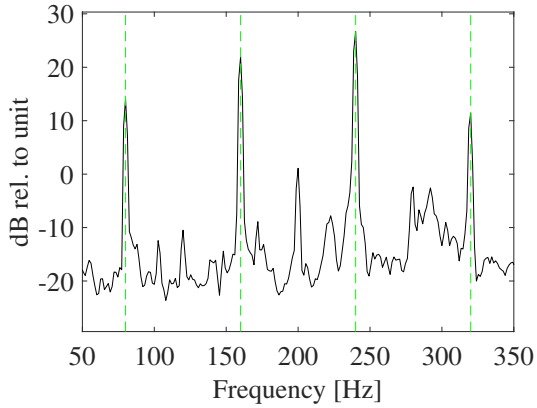

(a)

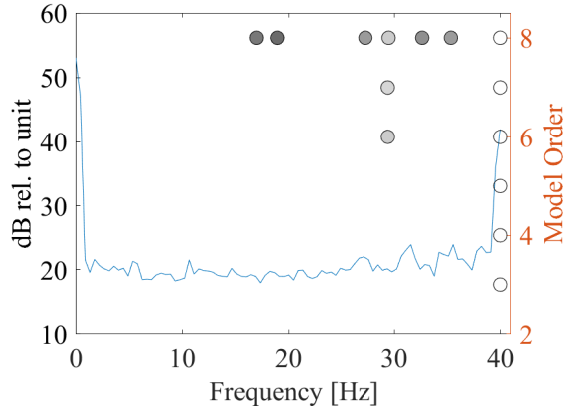

(b)

Figure 4.7: Auto PSD of the machining sound (a), stabilization diagrams (b) for: 2.7 mm at 2400 rev/min

DOC [mm]	Method	f [Hz]	SD	ζ [mean]	SD	μ_p	$\|\|\mu_p\|\|$
2.5	SDM	40	-	0.0142	-	-0.9562	0.956
	OMA	39.97	0.0497	0.0141	0.0048	-0.9567	0.956
2.7	SDM	40	-	0.0016	-	-0.994	0.994
	OMA	40	4e-7	0.0020	0.0013	-0.994	0.994

Table 4.3: Identified poles at 2400 rev/min.

4.2 MDOF experiments

The direct Frequency Response Function (FRF) at the tooltip and the cross-FRF between the tooltip and the location of the accelerometers on the spindle nose are shown in Fig. 4.9. The tool's deflections in both feed and Y-directions are dominated by one mode with the parameters shown in Table 4.4. The stability diagram of the setup, obtained by SDM, is shown in Fig. 4.8. All of the stability borders in this case show Hopf bifurcation and SDM does not detect any period-doubling bifurcation. The tested combinations of spindle speed and DOC are shown with circles for stable operations and crosses for unstable operations.

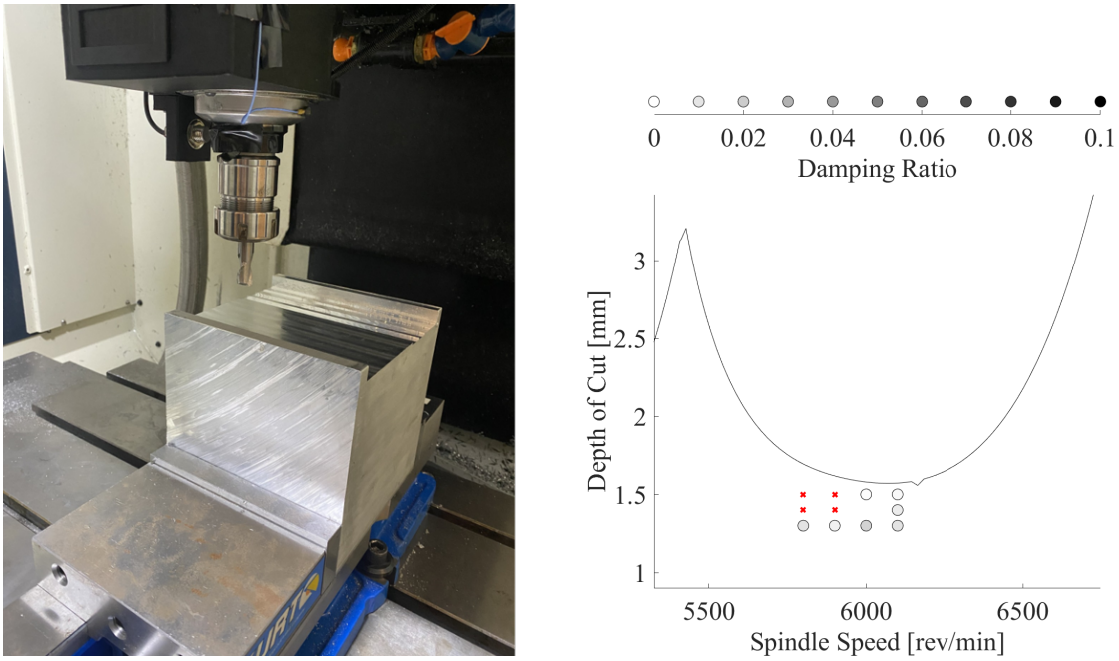

(a) (b)

Figure 4.8: a) MDOF experimental setup and b) SLD generated by the SDM.

Mode	Frequency[Hz]	Damping Ratio	Mode Shape [1/kg]
q	f	ζ	U
1	993.71	0.0235	[2.55, 0]
2	884.06	0.0326	[0, 2.63]

Table 4.4: Modal parameters of MDOF setup

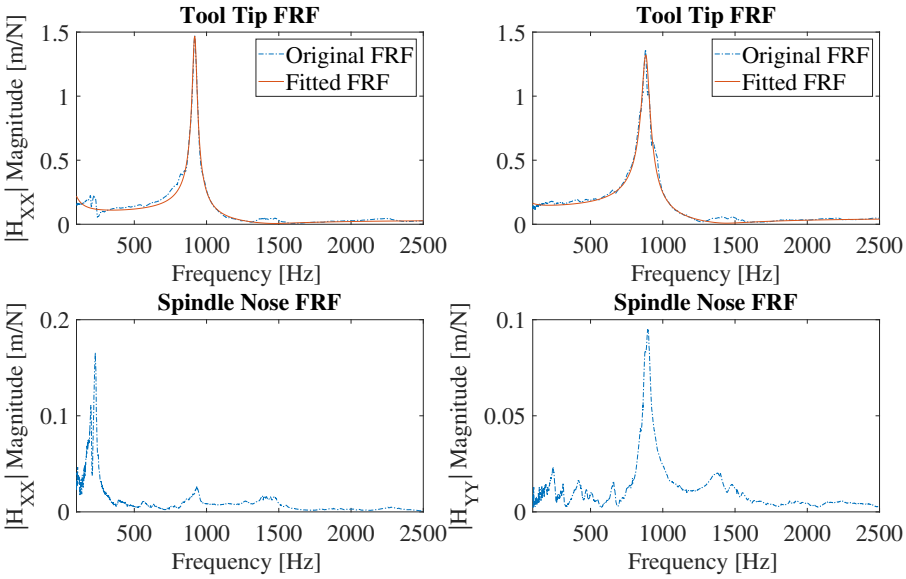

Figure 4.9: Tool tip and spindle nose FRFs. The subscripts of H stand for the excitation and measurement directions, respectively. Spindle nose FRFs are obtained by applying an impulse to the tool tip, and measuring the vibrations at the spindle nose.

As illustrated in Fig. 4.8b, tests conducted at 5800 and 5900 rev/min did not align with the stable region predicted by the SDM, while those at 6000 and 6100 rev/min exhibited a closer agreement. The OMA analysis for the case of 1.5 mm DOC and 6000 rev/min is presented in Fig. 4.10b. The sound PSD in part (a) of the figure shows the impending chatter frequency at 908 Hz. Consequently, a dominant pole at around 92 Hz is expected in the lifted response spectrum shown in part (b) of the figure. The stabilization diagram in part (b) reveals a dominant pole at 91.9 Hz with a damping ratio of 0.0010. This corresponds to $\mu = -0.96 + 0.25i$ in the discrete-time domain, with a modulus of 0.997, suggesting that a further increase in the depth of cut at 6000 rev/min may result in an unstable operation. Indeed, testing a 1.75 mm DOC at this spindle speed led to an unstable cut, as depicted in Fig. 4.10c. The comparison of the identified poles with SDM predictions for all of the tested DOC values at 6000 rev/min is shown in Table 4.5.

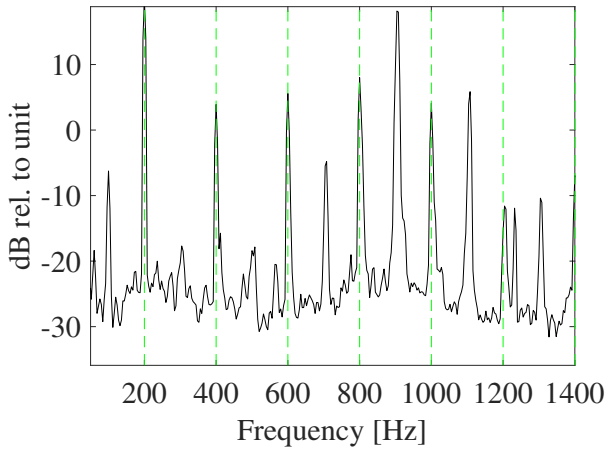

(a)

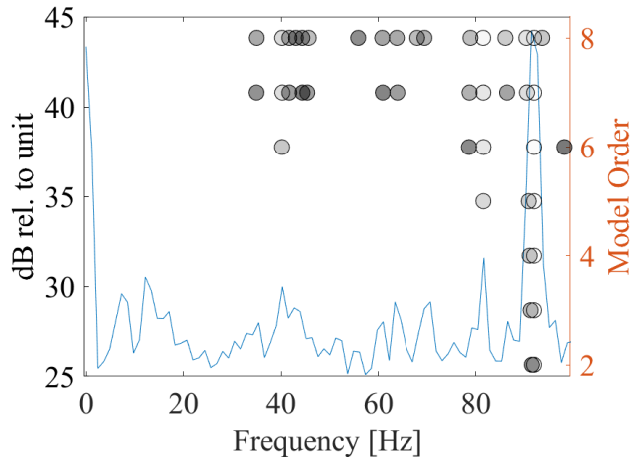

(b)

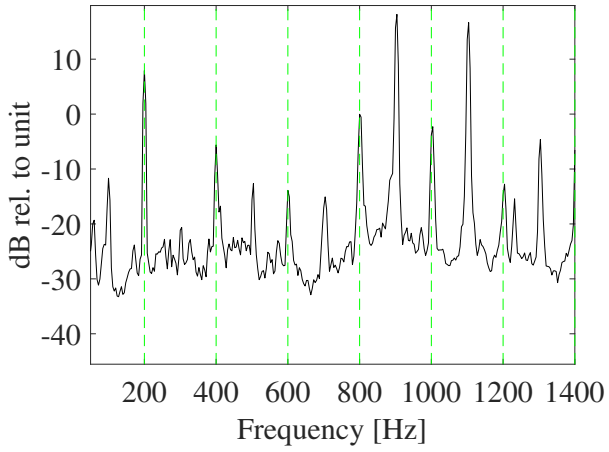

(c)

Figure 4.10: a) Auto PSD of the machining sound, b) stabilization diagram of the lifted response at 1.5 mm, 6000 rev/min. c) shows the auto PSD of the machining sound for the unstable operation at 1.75 mm, 6000 rev/min

DOC [mm]	Method	f [Hz]	SD	ζ [mean]	SD	μ_p	$\|\|\mu_p\|\|$
1.3	SDM	86.06	-	0.0682	-	-0.75 + 0.35i	0.832
	OMA	89.22	0.159	0.0091	0.0009	-0.92 + 0.32i	0.978
1.5	SDM	85.28	-	0.0229	-	-0.84 + 0.42i	0.940
	OMA	91.9	0.0131	0.0010	0.0003	-0.96 + 0.25i	0.997

Table 4.5: Identified poles at 6000 rev/min.

A set of tests were also conducted at 6100 rev/min, with depths of cut ranging from 1.3 mm to 1.5 mm. The stabilization diagrams for 1.3 mm and 1.5 mm DOC are presented together in Fig. 4.11, and the comparison of the identified poles against SDM predictions for all of the tested DOC values are shown in Table 4.6. The stabilization diagram in part (a) of Fig. 4.11 reveals a dominant pole at 98.6 Hz with a damping ratio of 0.0072. This corresponds to $\mu = -0.97 + 0.09i$ in the discrete-time domain, with a modulus of 0.978, suggesting that the depth of cut can be further increased. OMA identified a stable pole at 1.4 mm at the same spindle speed with 100.62 Hz frequency and 0.0045 damping ratio. This corresponds to $-0.98 + 0.03i$ with a modulus of 0.985 in discrete time domain. The modulus is close to 1, but OMA suggests that it can still be increased by a small amount before the operation becomes completely unstable. The identified pole at 1.5 mm at 6100 rev/min has a frequency of 101.667 Hz with a damping ratio of 0.0006. The discrete time modulus reads 0.998 suggesting that there is no room left in the stable zone and a further increase in the DOC might lead to unstable conditions. As suggested by the identified OMA pole at 1.5 mm, testing a 1.75 mm DOC at this spindle speed led to an unstable cut, as shown in Fig. 4.11c. The chatter frequency is 912 Hz according to the sound spectrum. The comparison of the identified poles with SDM predictions for all of the tested DOC values at 6100 rev/min is shown in Table 4.6.While the SDM does not predict period-doubling bifurcation, the OMA analysis shows period-doubling at 1.5 mm DOC.

DOC [mm]	Method	f [Hz]	SD	ζ [mean]	SD	μ_p	$\|\|\mu_p\|\|$
1.3	SDM	96.10	-	0.0567	-	-0.83 + 0.15i	0.85
	OMA	98.64	0.0545	0.0072	0.0050	-0.97 + 0.09i	0.978
1.4	SDM	95.87	-	0.0369	-	-0.92 + 0.17i	0.944
	OMA	100.62	0.0925	0.0046	0.0018	-0.98 + 0.03i	0.985
1.5	SDM	95.63	-	0.0183	-	-0.93 + 0.18i	0.948
	OMA	101.667	5e-4	0.0006	0.0002	-0.998	0.998

Table 4.6: Identified poles at 6100 rev/min.

Unlike the numerical simulations and the SDOF experimental results, in this generic milling test, discrepancies between the OMA and SDM results are substantial. The discrepancies at 6000 rev/min are limited to the predicted frequency and damping values; both SDM and OMA predict Hopf bifurcation. At 6100 re/min, in addition to the pole's frequency and damping, the two methods also deviate in the type of predicted bifurcation.

The stabilization diagrams of the stable points at 5800 and 5900 rev/min along with the sound PSD of the unstable points at those speeds are shown in Figs. 4.12 and 4.13. At these speeds, SDM predicts a higher stability than experimental observations. The predicted stability border is 1.7 mm and 1.6 mm in 5800 rev/min and 5900 rev/min, respectively. Nonetheless, consistent with the experimental observation, the OMA poles in the stable cases are close to 1 which indicates proximity to the stability border. OMA identifies $\mu = -0.59 + 0.80i$ with a modulus of 0.993 at 1.3 mm DOC and 5800 rev/min. Based on this modulus, the expectation is to encounter an unstable cut when operating with a higher DOC. Parallel to the expectation, the experiments showed an unstable point at 1.4 mm, 5800 rev/min as shown in Fig. 4.12b. Although the frequency and damping ratio do not match the SDM, predicted bifurcation types agree with the SDM results. Similar to the 5800 rev/min result, OMA identified $\mu = 0.78 + 0.60i$ with a modulus of 0.990 at 1.3 mm DOC and 5900 rev/min. The modulus is very close to 1 indicating that this DOC and spindle speed combination is very close to the stability border. 1.4 mm DOC at 5900 rev/min resulted in an unstable cut as can be seen in Fig. 4.13b.

The discrepancies between the OMA results and SDM predictions mainly stem from the variations in the system dynamics during the operations. The modal parameters in SDM are identified during zero spindle speed and without cutting forces. These parameters may vary when the spindle is spinning at a high speed and is subjected to high cutting forces. Errors

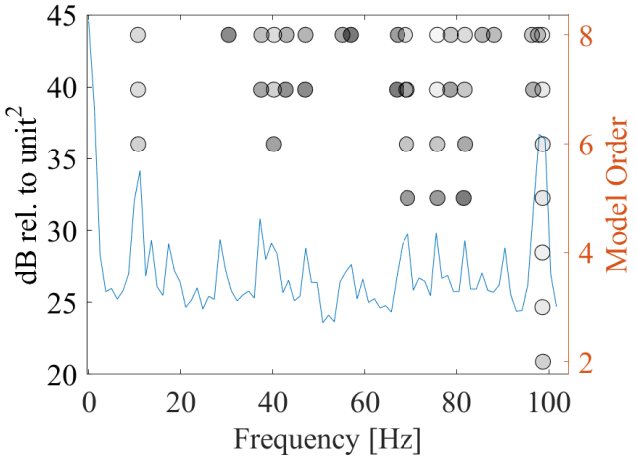

(a)

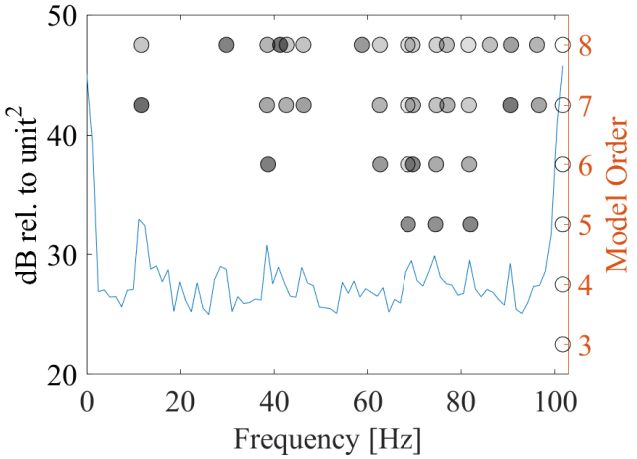

(b)

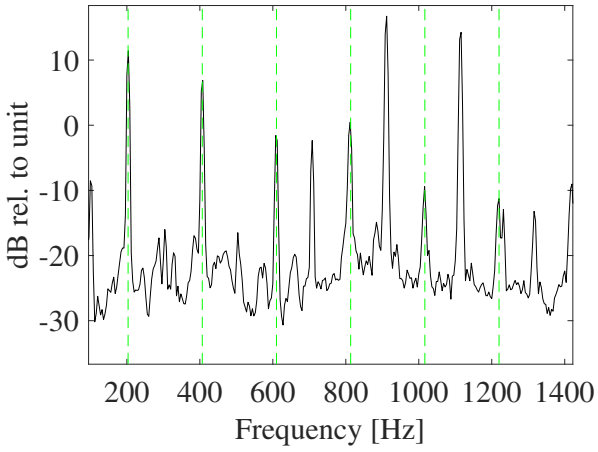

(c)

Figure 4.11: Stabilization diagrams (a,b) for: 1.3 mm and 1.5 mm at 6100 rev/min, respectively and c) the PSD of the sound at 1.75 mm at 6100 rev/min

in SLD predictions are commonly seen in practice and are usually attributed to inaccurate model parameters. In cases like 6000 rev/min or 6100 rev/min, the identified poles can be utilized to update the model parameters, enhancing chatter predictions [1]. In cases like 5800 rev/min or 5900 rev/min, where the model mispredicts stability, the identified poles can alarm proximity to the stability border to initiate corrective actions before vibrations become unstable.

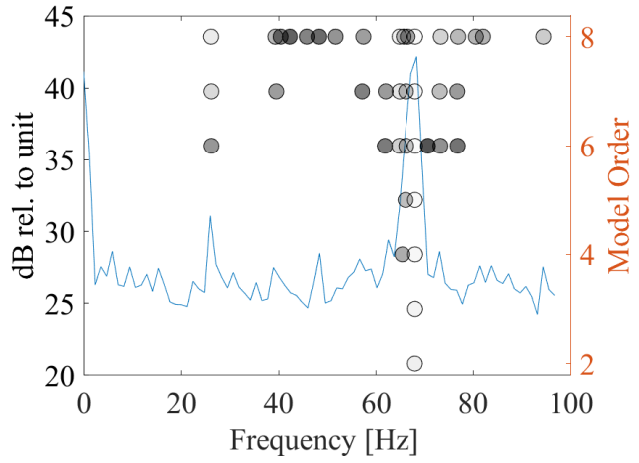

(a)

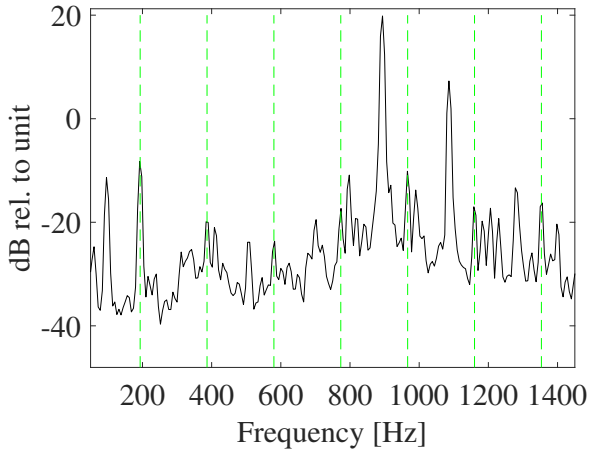

(b)

Figure 4.12: Stabilization diagram of the lifted response at 1.3 mm, 5800 rev/min (a) and auto PSD of the machining sound at 1.4 mm, 5800 rev/min (b)

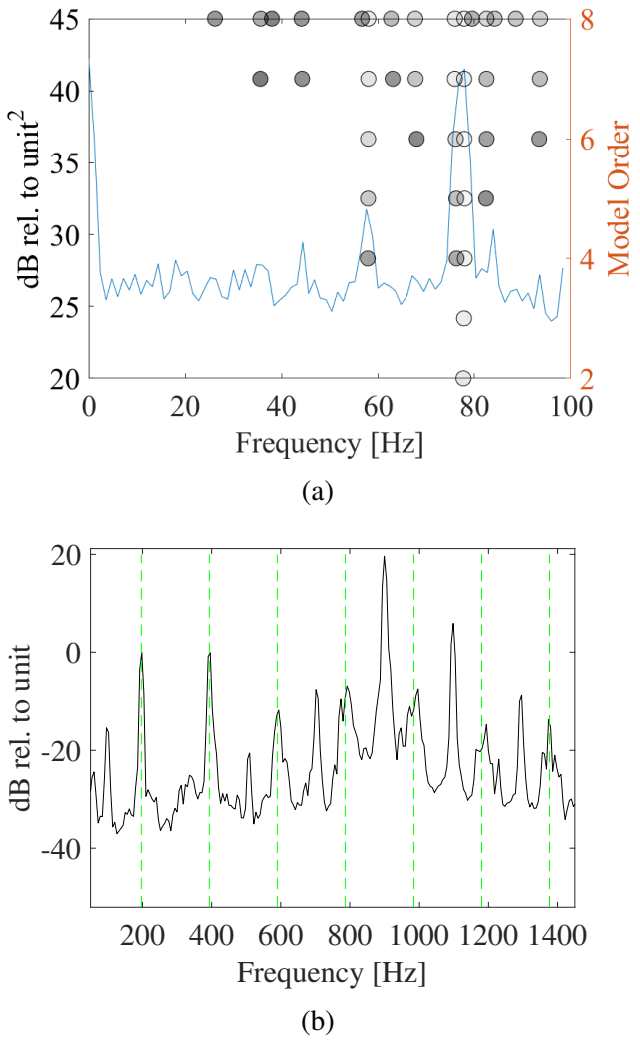

Figure 4.13: Stabilization diagram of the lifted response at 1.3 mm, 5900 rev/min (a) and auto PSD of the machining sound at 1.4 mm, 5900 rev/min (b)

4.3 Summary

In this chapter, the experimental results were presented. In the first case, a flexure was designed to mimic SDOF characteristics. Identified bifurcation types by the OMA and SDM were found to be the same. In the second case, a generic milling case with MDOF characteristics was studied. Considerable deviations between the identified poles and bifurcation types were observed at some spindle speeds and the reasons behind these deviations were discussed.

Chapter 5

Conclusion and Future Work

In this thesis, a new approach was introduced to estimate the dominant mode of the state transition matrix in milling using OMA and the lifting method by employing a one-per-revolution vibration measurement system. Milling dynamics were approximated through a finite-dimensional lumped system in the discrete-time domain, displaying linear time-periodic characteristics with a delay in the process. To employ OMA, which is suitable for only linear time-invariant processes, the system was lifted and all the periodicity was eliminated from its spectrum. The lifting method introduces virtual channels (or measurements) as if they were measured from different sensors. The overall lifted response, free of any periodicity, could be treated with any OMA method. In this thesis, the TDPR method was employed for system identification to identify the dominant Floquet multipliers of the delayed LTP dynamics in milling.

The method's performance was validated through both numerical simulations and experimental results. Also, a vibration measurement system was proposed for implementing the method in milling and its effectiveness was confirmed in standard operations. In experiments, lifting was accomplished through a data acquisition process involving a Hall-Effect sensor and a magnet. This ensured data capture at the same discrete instantaneous immersion angle points each time the acquisition started. This very specific task was applied by a dSpace MicroLabBox, where the triggers for rising edge and specific data sample count were defined. In both numerical and experimental cases, the method was proven to work well and the numerical results were cross-verified with the SDM results. It was observed that the changes in the parameters of the experimental setup due to material removal shifted the stability lobes. This proves the importance of in-process chatter monitoring to account for such deviations in the system parameters.

The proposed method proves capable of monitoring stability loss in the milling process

while it is still stable, by identifying the dominant pole of the state transition matrix of the linear time-periodic milling operation. The method is not applicable to very stable operations that have only tooth-passing frequency and its harmonics in their spectrum. Similarly, if the upcoming chatter frequency perfectly aligns with one of the harmonics, the method cannot identify the associated poles.

The presented method quantifies the process stability rather than just classifying it as stable or unstable. This advantage is critical for predicting chatter based on in-process observations while the system is still stable. However, in its current form, the presented OMA approach is not applicable for real-time process monitoring. Nonetheless, the method can be used to update the physics-based chatter model to enhance its chatter prediction accuracy. As well, it can be used to validate chatter models experimentally. Such validations are currently performed according to the dominant peaks in the process force, vibration, and sound spectra or surface roughness measurements. These subjective measures can now be enhanced by more concrete and quantitative criteria based on the experimentally identified Floquet multipliers.

Future studies will explore the online application, computational time reduction, and automation of the method. Automating the system identification component of the presented method and reducing its computational cost is key for enabling OMA-based process monitoring. Despite this, the current offline form demonstrates effectiveness in assessing machining process stability.

Bibliography

[1] K. Ahmadi. Bayesian updating of modal parameters for modeling chatter in turning. *CIRP Journal of Manufacturing Science and Technology*, 38:724–736, 2022.

[2] K. Ahmadi and Y. Altintas. Identification of machining process damping using output-only modal analysis. *Journal of Manufacturing Science and Engineering*, 136(5):051017, 2014.

[3] M. S. Allen. Frequency-Domain Identification of Linear Time-Periodic Systems Using LTI Techniques. *Journal of Computational and Nonlinear Dynamics*, 4(4):041004, Oct. 2009.

[4] Y. Altintas. *Manufacturing automation: metal cutting mechanics, machine tool vibrations, and CNC design*. Cambridge University Press, Cambridge ; New York, 2nd ed edition, 2012.

[5] Y. Altintas, G. Stepan, E. Budak, T. Schmitz, and Z. M. Kilic. Chatter stability of machining operations. *Journal of Manufacturing Science and Engineering*, 142(11):110801, 2020.

[6] Y. Altintas, G. Stépán, D. Merdol, and Z. Dombóvári. Chatter stability of milling in frequency and discrete time domain. *CIRP Journal of Manufacturing Science and Technology*, 1(1):35–44, 2008.

[7] B. Bamieh, J. B. Pearson, B. A. Francis, and A. R. Tannenbaum. A lifting technique for linear periodic systems with applications to sampled-data control. *Systems & Control Letters*, 17:79–88, 1991.

[8] B. A. Bamieh and J. B. Pearson. A general framework for linear periodic systems with applications to h/sup infinity/sampled-data control. *IEEE transactions on automatic control*, 37(4):418–435, 1992.

[9] P. Bayly, J. Halley, B. P. Mann, and M. Davies. Stability of interrupted cutting by temporal finite element analysis. *J. Manuf. Sci. Eng.*, 125(2):220–225, 2003.

[10] J. Berthold, M. Kolouch, J. Regel, and M. Dix. Identification of natural frequencies of machine tools during milling: comparison of the experimental modal analysis and the operational modal analysis. *Production Engineering*, pages 1–10, 2024.

[11] R. Brincker and C. E. Ventura. *Introduction to Operational Modal Analysis*. Wiley, 1 edition, Aug. 2015.

[12] E. Budak, Y. Altintas¸, and E. J. A. Armarego. Prediction of Milling Force Coefficients From Orthogonal Cutting Data. *Journal of Manufacturing Science and Engineering*, 118(2):216–224, 05 1996.

[13] H. Cherukuri, E. Perez-Bernabeu, M. Selles, and T. Schmitz. Machining chatter prediction using a data learning model. *Journal of Manufacturing and Materials Processing*, 3(2), 6 2019.

[14] G. Corson, J. Karandikar, and T. Schmitz. Physics-informed Bayesian machine learning case study: Integral blade rotors. *Journal of Manufacturing Processes*, 85(April 2022):503–514, 2023.

[15] T. Delio, J. Tlusty, and S. Smith. Use of Audio Signals for Chatter Detection and Control. *Journal of Engineering for Industry*, 114(2):146–157, May 1992.

[16] Y. Ding, L. Zhu, X. Zhang, and H. Ding. A full-discretization method for prediction of milling stability. *International Journal of Machine Tools and Manufacture*, 50(5):502–509, 2010.

[17] M. Farhadmanesh and K. Ahmadi. Online identification of mechanistic milling force models. *Mechanical Systems and Signal Processing*, 149:107318, 2021.

[18] D. Hajdu, F. Borgioli, W. Michiels, T. Insperger, and G. Stepan. Robust stability of milling operations based on pseudospectral approach. *International Journal of Machine Tools and Manufacture*, 149:103516, 2020.

[19] F. Hartung, T. Insperger, G. Stépán, and J. Turi. Approximate stability charts for milling processes using semi-discretization. *Applied Mathematics and Computation*, 174(1):51–73, Mar. 2006.

[20] A. Honeycutt and T. L. Schmitz. A new metric for automated stability identification in time domain milling simulation. *Journal of Manufacturing Science and Engineering, Transactions of the ASME*, 138(7), 2016.

[21] T. Insperger and G. Stépán. Updated semi-discretization method for periodic delay-differential equations with discrete delay. *International Journal for Numerical Methods in Engineering*, 61(1):117–141, 2004.

[22] T. Insperger and G. Stépán. *Semi-Discretization for Time-Delay Systems: Stability and Engineering Applications*. Springer, 04 2011.

[23] T. Insperger, G. Stépán, P. Bayly, and B. Mann. Multiple chatter frequencies in milling processes. *Journal of Sound and Vibration*, 262(2):333–345, Apr. 2003.

[24] J. Karandikar, A. Honeycutt, T. Schmitz, and S. Smith. Stability boundary and optimal operating parameter identification in milling using Bayesian learning. *Journal of Manufacturing Processes*, 56(February):1252–1262, 2020.

[25] S. Kim and K. Ahmadi. Estimation of vibration stability in turning using operational modal analysis. *Mechanical Systems and Signal Processing*, 130:315–332, Sept. 2019.

[26] A. K. Kiss, D. Hajdu, D. Bachrathy, G. Stepan, and Z. Dombovari. In-process impulse response of milling to identify stability properties by signal processing. *Journal of Sound and Vibration*, 527:116849, 2022.

[27] E. Kuljanic, G. Totis, and M. Sortino. Development of an intelligent multisensor chatter detection system in milling. *Mechanical Systems and Signal Processing*, 23(5):1704–1718, 2009.

[28] I. E. Minis, E. B. Magrab, and I. O. Pandelidis. Improved Methods for the Prediction of Chatter in Turning, Part 1: Determination of Structural Response Parameters. *Journal of Engineering for Industry*, 112(1):12–20, 02 1990.

[29] Y. Mohammadi and K. Ahmadi. In-process frequency response function measurement for robotic milling. *Experimental Techniques*, 47(4):797–816, 2023.

[30] O. Özşahin, E. Budak, and H. N. Özgüven. In-process tool point frf identification under operational conditions using inverse stability solution. *International Journal of Machine Tools and Manufacture*, 89:64–73, 2015.

[31] T. L. Schmitz. Chatter recognition by a statistical evaluation of the synchronously sampled audio signal. *Journal of Sound and Vibration*, 262(3):721–730, 2003.

[32] T. L. Schmitz. Chatter recognition by a statistical evaluation of the synchronously sampled audio signal. *Journal of Sound and Vibration*, 262(3):721–730, 2003.

[33] R. Teti, K. Jemielniak, G. O'Donnell, and D. Dornfeld. Advanced monitoring of machining operations. *CIRP Annals*, 59(2):717–739, 2010.

[34] J. Tlusty and M. Polacek. The Stability of Machine Tools against Self Excited Vibrations in Machining. *International research in production engineering*, pages 465–474, 1963.

[35] S. Tobias and W. Fischwick. Theory of Regenerative Machine Tool Chatter. *Engineer*, 205(7):199–203, 1958.

[36] F. Ulker. *A new framework for helicopter vibration suppression : time-periodic system identification and controller design*. Doctor of Philosophy, Carleton University, Ottawa, Ontario, 2011.

[37] M. Wan, J. Feng, Y.-C. Ma, and W.-H. Zhang. Identification of milling process damping using operational modal analysis. *International Journal of Machine Tools and Manufacture*, 122:120–131, Nov. 2017.

[38] I. Zaghbani and V. Songmene. Estimation of machine-tool dynamic parameters during machining operation through operational modal analysis. *International Journal of Machine Tools and Manufacture*, 49(12-13):947–957, 2009.